



Three-dimensional step potential electrochemical spectroscopy (SPECS) simulations of porous pseudocapacitive electrodes

Yucheng Zhou^a, Matevž Frajnkovič^a, Ampol Likitchatchawankun^{a,b}, Obaidallah Munteshari^{a,c}, Bing-Ang Mei^{a,d}, Laurent Pilon^{a,e,f,*}

^a Mechanical and Aerospace Engineering Department, Henry Samueli School of Engineering and Applied Science, University of California, Los Angeles, CA 90095, USA

^b Mechanical Engineering Simulation and Design Group, The Sirindhorn International Thai-German Graduate School of Engineering (TGGS), King Mongkut's University of Technology North Bangkok (KMUTNB), 1518 Parachart 1 Road, Wongsawang, Bangsue, Bangkok 10800, Thailand

^c Mechanical Engineering Department, King Fahd University of Petroleum and Minerals (KFUPM), Dhahran 31261, Saudi Arabia

^d School of Mechanical Engineering, Beijing Institute of Technology, Beijing 100081, China

^e California NanoSystems Institute, University of California, Los Angeles, CA 90095, USA

^f Institute of the Environment and Sustainability, University of California, Los Angeles, CA 90095, USA

ARTICLE INFO

Keywords:

Numerical simulations
Porous electrode
Electrochemical method
Pseudocapacitors
Electrochemical capacitors

ABSTRACT

This study validates the step potential electrochemical spectroscopy (SPECS) method and refines the associated analysis for differentiating the contributions of electrical double layer (EDL) formation and Faradaic reactions to the total charge storage in three-dimensional porous pseudocapacitive electrodes. The modified Poisson–Nernst–Planck (MPNP) model coupled with the Frumkin–Butler–Volmer theory were used to numerically reproduce experimental data obtained from the SPECS method accounting for interfacial, transport, and electrochemical phenomena in porous electrodes consisting of monodisperse spherical nanoparticles ordered in face-centered cubic (FCC) packing. The fitting analysis of the SPECS method was modified for the Faradaic current. The new model can accurately predict the individual contributions of EDL formation and Faradaic reactions to the total current. Moreover, the contributions of EDL formation at the electrode surface or at the electrode/electrolyte interface within the porous electrode can be identified. Similarly, the Faradaic reactions due to surface-controlled or diffusion-controlled mechanisms can be distinguished. Furthermore, the capacitance associated with EDL formation obtained from SPECS was in good agreement with that obtained from cyclic voltammetry. Finally, cyclic voltammograms were reconstructed using the multiple potential step chronoamperometry (MUSCA) method, and the integral capacitance associated with each charge storage mechanism was calculated for a range of scan rates.

1. Introduction

Electrochemical capacitors (ECs) form a promising category of electrical energy storage systems thanks to their large power density and long cycle life [1]. Based on the charging mechanism, ECs can be classified as electrical double layer capacitors (EDLCs) or pseudocapacitors [1,2]. Typically, EDLCs consist of carbon-based electrodes immersed in a liquid electrolyte and store charge physically via the electrical double layer (EDL) forming at the electrode/electrolyte interface [1,2]. Hybrid pseudocapacitors consist typically of a carbon-based and a redox-active electrode in a liquid electrolyte. In addition to EDL formation, pseudocapacitors store charge chemically via fast reduction/oxidation (redox) reactions [2,3]. The latter can be accompanied

by fast ion intercalation/deintercalation in/out of the redox-active materials without phase transition. Transition metal oxides (e.g., Nb₂O₅, MnO₂) have been widely studied as pseudocapacitive electrode materials due to their high theoretical capacity, chemical stability, and the reversibility of their redox reactions [4–6].

The most prevalent electrochemical techniques for characterizing the performance of ECs include cyclic voltammetry (CV), galvanostatic cycling (GC), and electrochemical impedance spectroscopy (EIS) [7]. More recently, the step potential electrochemical spectroscopy (SPECS) method has been proposed to determine the respective contributions of EDL formation and Faradaic reactions to the total charge storage in pseudocapacitive electrodes [8–10]. Furthermore, a method

* Corresponding author at: Mechanical and Aerospace Engineering Department, Henry Samueli School of Engineering and Applied Science, University of California, Los Angeles, CA 90095, USA.

E-mail address: pilon@seas.ucla.edu (L. Pilon).

<https://doi.org/10.1016/j.electacta.2024.144934>

Received 1 March 2024; Received in revised form 16 August 2024; Accepted 19 August 2024

Available online 22 August 2024

0013-4686/© 2024 The Authors. Published by Elsevier Ltd. This is an open access article under the CC BY-NC license (<http://creativecommons.org/licenses/by-nc/4.0/>).

Nomenclature

A	Surface area (nm ²)
A_{BET}	Total electrode/electrolyte interfacial area (nm ²)
$A_{BET,1}$	Geometric surface area of the electrode/electrolyte interface (nm ²)
$A_{BET,2}$	Porous surface area of the electrode/electrolyte interface (nm ²)
A_{fp}	Footprint surface area (nm ²)
a_i	Effective ion diameter of species i (nm)
C_1	Geometric surface EDL capacitance ($\mu\text{F cm}^{-2}$)
C_2	Porous surface EDL capacitance ($\mu\text{F cm}^{-2}$)
C_{diff}	Differential capacitance ($\mu\text{F cm}^{-2}$)
C_{int}	Integral capacitance ($\mu\text{F cm}^{-2}$)
C_s^{St}	Stern layer capacitance ($\mu\text{F cm}^{-2}$)
C_{EDL}	Total EDL capacitance ($\mu\text{F cm}^{-2}$)
$c_{1,P}$	Li ⁺ concentration in the electrode (mol L ⁻¹)
$c_{1,P,0}$	Initial Li ⁺ concentration in the electrode (mol L ⁻¹)
$c_{1,P,max}$	Maximum Li ⁺ concentration in the electrode (mol L ⁻¹)
c_i	Concentration of ion species i in the electrolyte (mol L ⁻¹)
c_∞	Ion concentration in the bulk electrolyte (mol L ⁻¹)
$D_{1,P}$	Diffusion coefficient of Li ⁺ ions in the electrode (m ² s ⁻¹)
D_i	Diffusion coefficient of ion species i in the electrolyte (m ² s ⁻¹)
e	Elementary charge, $e = 1.602 \times 10^{-19}$ C
F	Faraday constant, $F = eN_A = 9.648 \times 10^4$ C mol ⁻¹
H	Stern layer thickness (nm)
j	Magnitude of current density (A m ⁻²)
$j_{F,0}$	Exchange current density due to Faradaic reactions (A m ⁻²)
k_0	Reaction rate constant (m ^{2.5} mol ^{-0.5} s ⁻¹)
k_B	Boltzmann constant, $k_B = 1.38 \times 10^{-23}$ m ² kg s ⁻² K ⁻¹
L	Electrolyte domain thickness (nm)
L_C	Current collector thickness (nm)
L_P	Electrode thickness (nm)
N	Number of layers of electrode spherical particles
N_A	Avogadro number, $N_A = 6.022 \times 10^{23}$ mol ⁻¹
\mathbf{N}_i	Molar flux vector of ion species i (mol m ⁻² s ⁻¹)

associated with SPECS and named multiple potential step chronoamperometry (MUSCA) has been developed to reconstruct the electrode cyclic voltammograms with minimized ohmic polarization effects [11]. These characterization techniques have been demonstrated on devices ranging from small scale Swagelok cells [12] to large format pouch cells [13]. Previously, we validated theoretically both the SPECS and MUSCA methods for one-dimensional (1D) planar pseudocapacitive electrodes [14]. However, the 1D model did not capture the microporous and mesoporous structures prevailing in actual pseudocapacitive electrode materials [15–17].

N_s	Number of data points per potential step
\mathbf{n}	Normal vector of a surface
n_c	Cycle number
n_s	Total number of potential steps
p_s	Potential step number
ΔQ_F	Total amount of charge stored due to the Faradaic current (C)
R_1	Geometric surface electrical double layer resistance ($\Omega \text{ cm}^2$)
R_2	Porous surface electrical double layer resistance ($\Omega \text{ cm}^2$)
R_{ct}	Charge transfer resistance ($\Omega \text{ cm}^2$)
R_d	Diffusion resistance ($\Omega \text{ cm}^2$)
R_{EDL}	Total electrical double layer resistance ($\Omega \text{ cm}^2$)
R_u	Universal gas constant, $R_u = 8.314$ J mol ⁻¹ K ⁻¹
r	Radius of electrode spherical particles (nm)
\mathbf{r}	Location in three-dimensional space (nm)
\mathbf{r}_{cl}	Device centerline location (nm)
$\mathbf{r}_{C/E}$	Current collector/electrolyte interface location (nm)
$\mathbf{r}_{E/E}$	Electrode/electrolyte interface location (nm)
\mathbf{r}_H	Stern/diffuse layer interface location (nm)
T	Temperature (K)
t	Time (s)
t_{cd}	Charging/discharging cycle period (s)
t_e	Equilibration time (s)
t_t	Transition time (s)
t_w	Time window in the MUSCA method (s)
Δt	Time step (data acquisition time) (s)
z_i	Valency of ion species i

Greek symbols

α	Transfer coefficient
δ	Objective function
ϵ_0	Vacuum permittivity, $\epsilon_0 = 8.854 \times 10^{-12}$ F m ⁻¹
ϵ_r	Relative permittivity of the electrolyte
η	Overpotential (V)
Λ	Electrochemical Biot number
ν	Scan rate (V s ⁻¹)
ψ	Electric potential (V)
ψ_s	Potential vs. Ag/AgCl at the current collector/electrode interface (V)
$\psi_{s,min}, \psi_{s,max}$	Minimum and maximum of the potential window vs. Ag/AgCl (V)
$\Delta\psi_{eq}$	Equilibrium potential difference vs. Ag/AgCl (V)

This study aims to numerically validate and, if necessary, modify the SPECS method for three-dimensional (3D) mesoporous pseudocapacitive electrodes. Numerical simulations were based on the modified Poisson–Nernst–Planck (MPNP) model coupled with the Frumkin–Butler–Volmer theory. In addition, the SPECS method was combined with the MUSCA method to identify the contributions of EDL formation and Faradaic reactions to the total current density and to provide physical interpretation of the fitting parameters.

$\Delta\psi_{eq,0}$	Initial equilibrium potential difference vs. Ag/AgCl (V)
$\Delta\psi_H$	Potential drop across the Stern layer (V)
$\Delta\psi_s$	Potential step (V)
σ_C	Current collector electrical conductivity (S m ⁻¹)
σ_P	Electrode electrical conductivity (S m ⁻¹)
τ	Time constant (s)
τ_d	Diffusion time constant (s)

Superscripts and subscripts

<i>BET</i>	Refers to the electrode/electrolyte interface
<i>EDL</i>	Refers to the electrical double layer
<i>EDL1</i>	Refers to the geometric surface EDL
<i>EDL2</i>	Refers to the porous surface EDL
<i>F</i>	Refers to the Faradaic contribution
<i>F1</i>	Refers to the surface-controlled Faradaic contribution
<i>F2</i>	Refers to the diffusion-controlled Faradaic contribution
<i>f_p</i>	Refers to the footprint surface
<i>M</i>	Refers to the MUSCA method
<i>n</i>	Refers to the normal component of a vector
<i>r</i>	Refers to the residual component
<i>S</i>	Refers to the SPECS method
<i>T</i>	Refers to the total component

2. Background

2.1. SPECS method

Chronoamperometry is a family of techniques where a step function is applied to the potential of the working electrode as the current response is recorded. The current response to each potential step is typically a decay as a function of time and can be analyzed to distinguish the various charge storage mechanisms of the working electrode [7]. The most common example is the double potential step chronoamperometry where the imposed potential consists of a single step up and step down in sequence [7]. Multiple variants of chronoamperometry have also been developed over time, such as the double potential step chronocoulometry. In this case, instead of the current response, the integral of the current versus time is recorded corresponding to the amount of charge passed. Here, the response in the charge passage can equally be analyzed to separate the contributions of EDL formation and Faradaic reactions to the total amount of charge storage [7]. One latest adaptation of chronoamperometry is the SPECS method. The SPECS method consists of imposing a series of small potential steps $\Delta\psi_s$ on a pseudocapacitor within a potential window from $\psi_{s,min}$ to $\psi_{s,max}$ and measuring the total footprint current density response $j_T(t)$ (in A/m²) at each potential step defined per unit footprint surface area A_{f_p} of the current collector [18–20]. This method has been developed to identify the contributions of EDL formation and Faradaic reactions to the total current in pseudocapacitive electrodes [8–10]. Dupont and Donne [8–10] suggested that the total current density response to an imposed potential step in a porous pseudocapacitive electrode should be fitted to a function $j_T^S(t)$ expressed as the sum of an EDL current density $j_{EDL}^S(t)$, a Faradaic current density $j_F^S(t)$, and a residual current density $j_r^S(t)$, i.e.,

$$j_T^S(t) = j_{EDL}^S(t) + j_F^S(t) + j_r^S(t). \quad (1)$$

The EDL current density $j_{EDL}^S(t)$ was further divided into two contributions from EDL formation (i) at the so-called geometric surface

defined as the interface of the electrode with the bulk electrolyte and (ii) at the interfacial surface of micropores and mesopores within the porous electrode, represented by $j_{EDL1}^S(t)$ and $j_{EDL2}^S(t)$, respectively [8–10]. Here, $j_{EDL1}^S(t)$ and $j_{EDL2}^S(t)$ were modeled based on an equivalent circuit of a resistor and a capacitor in series so that [8–10],

$$j_{EDL}^S(t) = j_{EDL1}^S(t) + j_{EDL2}^S(t) = \frac{\Delta\psi_s}{R_1} \exp\left(-\frac{t}{R_1 C_1}\right) + \frac{\Delta\psi_s}{R_2} \exp\left(-\frac{t}{R_2 C_2}\right) \quad (2)$$

where R_1 , C_1 and R_2 , C_2 are the resistances and capacitances due to EDL formation at the geometric surface denoted by $A_{BET,1}$ and at the inner porous electrode/electrolyte interface denoted by $A_{BET,2}$ (see Fig. 1 for illustration). Furthermore, the total EDL resistance R_{EDL} and the total EDL capacitance C_{EDL} were expressed as [8–10],

$$R_{EDL} = \frac{R_1 R_2}{R_1 + R_2} \quad \text{and} \quad C_{EDL} = C_1 + C_2. \quad (3)$$

On the other hand, the Faradaic current density $j_F^S(t)$ was modeled based on Fick's second law of diffusion in spherical coordinates as [8–10],

$$j_F^S(t) = \frac{6\Delta Q_F}{\tau_d A} \sum_{n=1}^{\infty} \exp\left(-\frac{n^2 \pi^2 t}{\tau_d}\right). \quad (4)$$

Here, A is the surface area over which the current density is averaged (i.e., either the footprint surface area A_{f_p} of the current collector or the total electrode/electrolyte interfacial area A_{BET}), while ΔQ_F and τ_d are the total amount of charge stored due to the Faradaic reactions and the diffusion time constant respectively expressed as [21,22],

$$\Delta Q_F = \int_t^{t+\Delta t} j_F^S(t) A dt = -\frac{F A_{BET} r \Delta c_{1,P}}{3} \quad \text{and} \quad \tau_d = \frac{r^2}{D_{1,P}} \quad (5)$$

where $F = eN_A = 9.648 \times 10^4$ C mol⁻¹ is the Faraday constant, r is the average radius of redox-active spherical particles making up the electrode, $\Delta c_{1,P}$ is the net concentration change of cations in the electrode due to the potential step, and $D_{1,P}$ is the diffusion coefficient of cations in the redox-active materials. After a sufficiently long relaxation duration (i.e., $t \gg \tau_d$), the high order terms ($n > 1$) in Eq. (4) are negligible leading to [22,23],

$$j_F^S(t) = \frac{6\Delta Q_F}{\tau_d A} \exp\left(-\frac{\pi^2 t}{\tau_d}\right). \quad (6)$$

This model is representative of diffusion-controlled Faradaic reactions only.

Alternatively, Montella [22] proposed a model for $j_F^S(t)$ accounting for finite interfacial charge transfer kinetics given by,

$$j_F^S(t) = \frac{6\Delta Q_F}{\tau_d A} \sum_{n=1}^{\infty} \frac{A^2}{A^2 - A + b_n^2} \exp\left(-\frac{b_n^2 t}{\tau_d}\right). \quad (7)$$

Here, b_n is the n th root of the following equation [22,24],

$$b_n \cot b_n + A - 1 = 0 \quad (8)$$

where A is the electrochemical Biot number expressed as [22,24],

$$A = -\frac{r j_{F,0}}{D_{1,P} R_u T} \frac{\partial \Delta\psi_{eq}}{\partial c_{1,P}} = \frac{R_d}{R_{ct}}. \quad (9)$$

Here, $j_{F,0}$ is the exchange current density, $R_u = 8.314$ J mol⁻¹ K⁻¹ is the universal gas constant, T is the temperature, $\Delta\psi_{eq}$ is the equilibrium potential difference (i.e., the potential difference between the electrode and the electrolyte across their interface at zero net reaction rate), $c_{1,P}$ is the concentration of cations in the electrode, R_d and R_{ct} are the diffusion and interfacial charge transfer resistances, respectively. Here also, after a sufficiently long relaxation duration (i.e., $t \gg \tau_d$), the high

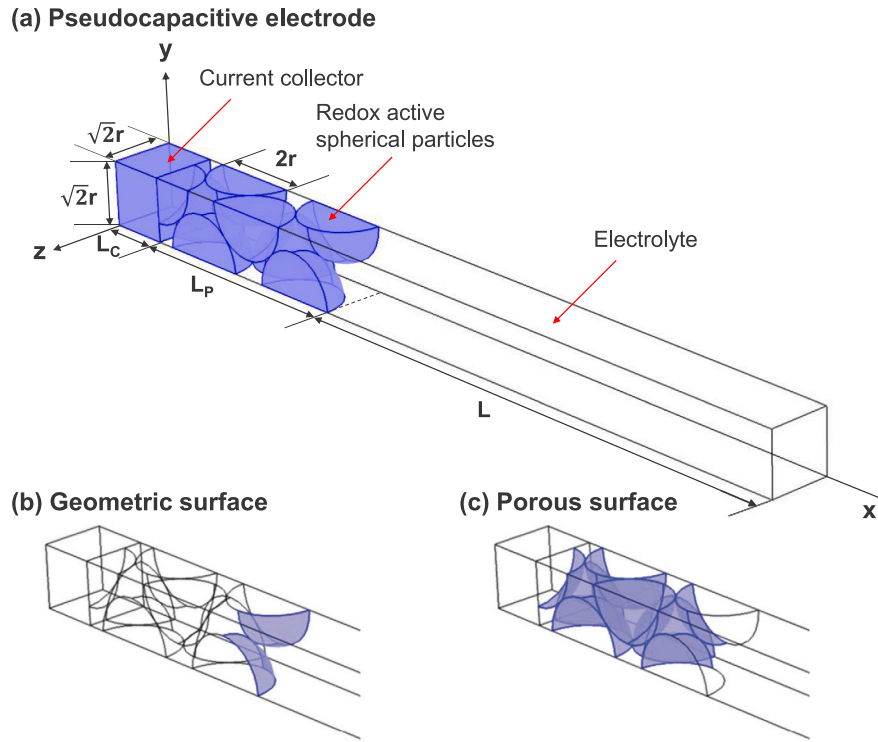


Fig. 1. (a) Schematic, coordinate system, and dimensions of the simulated 3D mesoporous pseudocapacitive electrode consisting of monodisperse spherical particles of radius r ordered in face-centered cubic (FCC) packing supported by a planar current collector in an electrolyte containing Li^+ ions in a three-electrode configuration with Ag/AgCl as the reference electrode. (b) Geometric surface area $A_{BET,1}$ and (c) porous surface area $A_{BET,2}$ of the electrode/electrolyte interface.

order terms ($n > 1$) in Eq. (7) become negligible leading to [22,23],

$$j_F^S(t) = \frac{6\Delta Q_F}{\tau_d A} \frac{\Lambda^2}{\Lambda^2 - \Lambda + b_1^2} \exp\left(-\frac{b_1^2 t}{\tau_d}\right) = P_1 \exp(-P_2 t) \quad (10)$$

where the fitting parameters P_1 and P_2 can be identified as,

$$P_1 = \frac{6\Delta Q_F}{\tau_d A} \frac{\Lambda^2}{\Lambda^2 - \Lambda + b_1^2} \quad \text{and} \quad P_2 = \frac{b_1^2}{\tau_d}. \quad (11)$$

The value of Λ characterizes the main limitation for the rate of Faradaic reactions. For diffusion-controlled processes, $R_d \gg R_{ct}$, $\Lambda \gg 1$, and $b_1 = \pi$, so that Eq. (10) reduces to Eq. (6) [22,24]. By contrast, when processes are controlled by finite interfacial charge transfer kinetics, $R_d \ll R_{ct}$, $\Lambda \ll 1$, and $b_1 \simeq \sqrt{3}\Lambda$ [22,24]. Finally, the residual current density $j_r^S(t)$ is a constant accounting for electrolyte decomposition reactions and/or parasitic reactions in the electrode material [8–10]. Note, however, that the above expressions for the different contributions to the total current density $j_T(t)$ have been previously validated theoretically for 1D homogeneous electrodes but not for 3D heterogeneous porous pseudocapacitive electrodes.

2.2. MUSCA method

The MUSCA method aims to explicitly quantify the contributions of different charge storage mechanisms to the total capacitance. It has proved effective in correcting for ohmic polarization effects and the drift of redox peaks with increasing scan rate typically observed in CV measurements [11,14]. Similar to SPECS, MUSCA starts by imposing a series of small potential steps $\Delta\psi_s$ within a potential window from $\psi_{s,min}$ to $\psi_{s,max}$ and measuring the total current density response $j_T(t)$ to each potential step. Then, for a given scan rate ν , $j_T(t)$ is averaged over a certain time window t_v defined from the beginning of the potential step

$\Delta\psi_s$ to obtain the mean current density $j_T^A(\psi_s)$ at potential ψ_s as [11],

$$j_T^A(\psi_s) = \frac{1}{t_v} \int_0^{t_v} j_T(t) dt \quad (12)$$

where superscript “A” refers to the mean current density from the MUSCA method, and t_v is chosen according to [11],

$$t_v = \frac{\Delta\psi_s}{\nu}. \quad (13)$$

Finally, cyclic voltammograms with minimized ohmic polarization effects are reconstructed by plotting $j_T^A(\psi_s)$ vs. ψ_s [11].

2.3. Application of the SPECS and MUSCA methods

Both the SPECS and MUSCA methods have been employed in a wide range of applications. For example, Forghani et al. [12] used the SPECS method to identify the geometric and porous capacitances during the electrochemical characterization of symmetrical activated carbon electrochemical capacitors with organic electrolyte. The MUSCA method was used to quantify the performance over a range of scan rates, both for the entire device and for each individual electrode. Subsequently, the authors assembled prototype pouch cells using the same electrode and electrolyte materials and evaluated their electrochemical behavior [13]. Here, the temporal evolution of the fitting parameters retrieved from SPECS and the rate performance from MUSCA were combined to identify issues within the cell including leakage current, cell degradation, and electrolyte depletion.

In another study, the SPECS and MUSCA methods were used to optimize experimentally electrolytic amorphous carbon as electrode materials by distinguishing and quantifying the EDL and pseudocapacitive contributions at different scan rates [25]. A similar study applied the SPECS and MUSCA methods to demonstrate that the capacitive charge storage in glassy carbon electrodes was better with non-aqueous

electrolytes than with aqueous electrolytes due to ion solvation [26]. In fact, the study compared the fitted total EDL resistance R_{EDL} and total EDL capacitance C_{EDL} between the same electrodes in different electrolytes. Based on those results, the authors reasoned that the solvation shells surrounding the adsorbing ions in aqueous electrolytes not only increased resistance but also inhibited denser packing of ions at the electrode surface, thus decreasing the capacitive charge storage.

Another study utilized both the SPECS and MUSCA methods in place of conventional CV measurements to validate experimentally the two methods and simultaneously investigate the charge storage mechanisms in four electrochemical capacitor systems [27]. The Swagelok cells consisted of activated carbon, RuO₂, MnO₂, or Ni(OH)₂ working electrodes and activated carbon counter electrodes in alkaline electrolytes. In addition, Forghani et al. [28] used CV, EIS, SPECS, and MUSCA methods to analyze the semiconducting properties of electrolytic MnO₂ deposited on titanium substrates as electrodes for electrochemical capacitors. Here, SPECS combined with EIS enabled the determination of electronic properties across the full potential window, identifying both n-type and p-type behavior in the electrolytic MnO₂ electrodes. Furthermore, in two separate studies the SPECS and MUSCA methods provided mechanistic insights into the microstructures of various porous carbon electrodes [29,30]. Of particular value was their ability to reveal the capacitances associated with EDL formation at the geometric surface or at the porous surface in each unique porous structure.

Overall, the SPECS and MUSCA methods give an unmatched capability to distinguish and quantify the charge storage contributions from various mechanisms using relatively simple experimental procedures applicable to most electrochemical systems. These methods have been validated qualitatively using experimental data. This study aims to rigorously validate the SPECS method and the MUSCA method, using state-of-the-art physical modeling and numerical simulations, to quantify the contributions, to the total current density, of EDL formation and Faradaic reactions occurring at the surface or within 3D pseudocapacitive electrodes.

3. Analysis

3.1. Schematic and assumptions

Fig. 1(a) shows the schematic of the simulated 3D mesoporous pseudocapacitive electrode consisting of monodisperse spherical particles of radius r ordered in face-centered cubic (FCC) packing supported by a planar current collector in an electrolyte containing Li⁺ ions in a three-electrode configuration with Ag/AgCl as the reference electrode. The example shown here had a number of particle layers $N = 3.5$. The current collector, electrode, and electrolyte domain thicknesses were denoted by L_C , L_p , and L , respectively. Fig. 1(b) shows the geometric surface area $A_{BET,1}$ corresponding to the exterior electrode surface with direct access to the bulk electrolyte. Fig. 1(c) shows the interior electrode/electrolyte interface also known as the porous surface area $A_{BET,2}$ [8–10].

To make the problem mathematically tractable, the following assumptions were made: (1) The electrolyte was binary and symmetric, i.e., it consisted of two ion species of opposite valency $\pm z$. (2) Cations and anions had the same effective diameter a and diffusion coefficient D in the electrolyte [31,32]. (3) The Stern layer contained no free charge and its thickness H was approximated as the effective radius of the ions, so that $H = a/2$ [7,33,34]. (4) The transport properties of the electrode and electrolyte were taken as constant and independent of state-of-charge. (5) Bulk motion of the electrolyte was negligible. (6) Ion intercalation/deintercalation in/out of the electrode spherical particles was modeled as a diffusion process. (7) The temperature T was uniform in the simulated domain and constant over time. (8) Electrical contact resistance between the current collector and the electrode, and between the electrode spherical particles, was negligible. (9) Residual current density associated with electrolyte decomposition

reactions and/or parasitic reactions in the electrode material was ignored, i.e., $j_r^S(t) = 0$. (10) Current arising from EDL formation at the current collector/electrolyte interface was negligible compared to that at the electrode/electrolyte interface.

3.2. Governing equations

The modified Poisson–Nernst–Planck (MPNP) model coupled with the Frumkin–Butler–Volmer theory were used to numerically reproduce experimental data obtained from the SPECS method accounting for interfacial, transport, and electrochemical phenomena in the simulated domain [35]. The governing equations have been described in our previous studies [36–38] and are reproduced in Supplementary Materials for the sake of completeness (see Section S.1). In brief, the spatiotemporal evolution of (i) the local electric potential $\psi(\mathbf{r}, t)$ in the current collector, the electrode, and the electrolyte, as well as (ii) the local concentrations $c_1(\mathbf{r}, t)$ of cations and $c_2(\mathbf{r}, t)$ of anions in the electrolyte were governed by the MPNP model [36–38]. The local concentration $c_{1,p}(\mathbf{r}, t)$ of Li⁺ ions in the electrode was governed by the 3D transient mass diffusion equation [39–41].

3.3. Initial and boundary conditions

All initial and boundary conditions necessary to solve the 3D transient governing equations are described in detail in Supplementary Materials (see Section S.2). The potential at the current collector surface $(0, y, z)$ was imposed as a multi-step function for SPECS simulations according to [14],

$$\psi_s(0, y, z, t) = \begin{cases} \psi_{s,min} + (p_s - 1)\Delta\psi_s & \text{for } 1 \leq p_s \leq (n_s + 1)/2 \text{ (charging)} \\ \psi_{s,max} - (p_s - \frac{n_s+1}{2})\Delta\psi_s & \text{for } (n_s + 1)/2 \leq p_s \leq n_s \text{ (discharging)} \end{cases} \quad (14)$$

where $\psi_{s,min}$ and $\psi_{s,max}$ are the minimum and maximum of the potential window, respectively. Here, p_s is the potential step number and n_s is the total number of potential steps $\Delta\psi_s$ to cover the entire potential window, i.e., $n_s = [2(\psi_{s,max} - \psi_{s,min})/\Delta\psi_s] + 1$, with each step lasting an equilibration time of t_e .

On the other hand, for simulating cyclic voltammograms, the potential at the current collector surface $(0, y, z)$ was imposed as a triangular function of time t given by [42],

$$\psi_s(0, y, z, t) = \begin{cases} \psi_{s,min} + v[t - (n_c - 1)t_{cd}] & \text{for } (n_c - 1)t_{cd} \leq t < (n_c - 1/2)t_{cd} \text{ (charging)} \\ \psi_{s,max} - v[t - (n_c - 1/2)t_{cd}] & \text{for } (n_c - 1/2)t_{cd} \leq t < n_c t_{cd} \text{ (discharging)} \end{cases} \quad (15)$$

where n_c is the cycle number, t_{cd} is the cycle period, and v is the scan rate, i.e., $v = 2(\psi_{s,max} - \psi_{s,min})/t_{cd}$.

3.4. Constitutive relationships

The present study used realistic material properties summarized in Table 1 and taken from the literature for the current collector, the porous pseudocapacitive electrode consisting of Nb₂O₅ nanoparticles [7,43–45], and the electrolyte consisting of 1 M LiClO₄ salt in propylene carbonate (PC) solvent [46,47]. The thickness of the current collector was taken as $L_C = 10$ nm with electrical conductivity $\sigma_C = 5$ S m⁻¹ corresponding to carbon-based materials [48]. The electrodes were made of spherical particles with radius $r = 3.75$ nm, while the number of particle layers N varied between 2.5 and 4.5 for different cases of the parametric study (3.5 for the baseline case), resulting in

Table 1

Values or ranges of current collector, electrode, and electrolyte dimensions and properties used in the simulations reported in this study.

Variable	Symbol	Value	Unit
Effective ion diameter	a	0.67	nm
Initial ion concentration in the electrode	$c_{1,P,0}$	6.58	mol L ⁻¹
Maximum ion concentration in the electrode	$c_{1,P,max}$	32.9	mol L ⁻¹
Ion concentration in the bulk electrolyte	c_∞	1	mol L ⁻¹
Ion diffusion coefficient in the electrolyte	D	2×10^{-11}	m ² s ⁻¹
Ion diffusion coefficient in the electrode	$D_{1,P}$	10^{-14} – 10^{-12}	m ² s ⁻¹
Reaction rate constant	k_0	10^{-10} – 10^{-8}	m ^{2.5} mol ^{-0.5} s ⁻¹
Electrolyte domain thickness	L	100	nm
Current collector thickness	L_C	10	nm
Electrode thickness	L_P	14.4–25.0	nm
Number of layers of electrode spherical particles	N	2.5–4.5	
Radius of electrode spherical particles	r	3.75	nm
Temperature	T	293	K
Valency	z	1	
Transfer coefficient	α	0.5	
Relative permittivity of the electrolyte	ϵ_r	64.4	
Potential window vs. Ag/AgCl	$\psi_{s,min}$	0	V
	$\psi_{s,max}$	0.4	V
Electrical conductivity of the current collector	σ_C	5	S m ⁻¹
Electrical conductivity of the electrode	σ_P	10^{-4}	S m ⁻¹

electrode thicknesses L_P ranging from 14.4 to 25.0 nm (19.7 nm for the baseline case). The capacitance of the electrodes quantitatively varied with both the radius of electrode spherical particles r and the number of particle layers N . Note that the purpose of this study is to validate the SPECS and MUSCA methods under numerically controlled conditions. Therefore, the dimensions selected were smaller than typical experiments in order to reduce the computational resources and time required to perform the numerous simulations. The electrode electrical conductivity was taken as $\sigma_P = 10^{-4}$ S m⁻¹ [15] and the reaction rate constant k_0 varied between 10^{-10} and 10^{-8} m^{2.5} mol^{-0.5} s⁻¹ for different cases of the parametric study (10^{-10} m^{2.5} mol^{-0.5} s⁻¹ for the baseline case) [43,49,50]. For electrodes consisting of transition metal oxides, the equilibrium potential difference $\Delta\psi_{eq}$ is typically determined experimentally as a function of the state-of-charge (SOC) defined as $c_{1,P}/c_{1,P,max}$ by fitting experimental data for open-circuit potential [51–53]. In the absence of experimental data for Nb₂O₅, $\Delta\psi_{eq}$ was modeled as a linear function of SOC as measured for 100 μm thick MnO₂ dense films vs. Ag/AgCl reference electrode and expressed as [44],

$$\Delta\psi_{eq}(t) = 10.5[4 - c_{1,P}(t)/c_{1,P,max}] - 39.9. \quad (16)$$

Here, the maximum Li⁺ ion concentration $c_{1,P,max} = 32.9$ mol L⁻¹ corresponded to fully lithiated manganese dioxide LiMnO₂ [45], and the initial Li⁺ ion concentration $c_{1,P,0} = 6.58$ mol L⁻¹ was such that the initial equilibrium potential difference $\Delta\psi_{eq,0}$ was zero. The transfer coefficient α in the Frumkin–Butler–Volmer equation was assumed to be 0.5 to consider the ideal case of identical energy barriers for forward and backward reversible redox reactions [7]. The diffusion coefficient $D_{1,P}$ of Li⁺ ions in transition metal oxides typically ranges from 10^{-16} to 10^{-10} m² s⁻¹ [43]. Here, $D_{1,P}$ varied between 10^{-14} and 10^{-12} m² s⁻¹ for different cases of the parametric study (10^{-14} m² s⁻¹ for the baseline case). The thickness of the electrolyte domain was taken as $L = 100$ nm with bulk ion concentration $c_\infty = 1$ mol L⁻¹ and valency $z = 1$. The electrolyte relative permittivity was set to that of PC with $\epsilon_r = 64.4$ [46]. The effective ion diameter and the ion diffusion coefficient of both Li⁺ and ClO₄⁻ ions were set to those of solvated Li⁺ ions in PC with $a = 0.67$ nm and $D = 2 \times 10^{-11}$ m² s⁻¹, respectively [47]. Finally, the temperature was set to $T = 293$ K, and the potential window ranged from $\psi_{s,min} = 0$ V to $\psi_{s,max} = 0.4$ V. This potential window covered both the Faradaic and the capacitive regimes for the simulated electrode [39]. Specifically, the Faradaic regime consisted of potentials below 0.2 V where the interfacial charge transfer kinetics was more favorable for Faradaic reactions to occur, and vice versa for the capacitive regime. In fact, as the potential approached 0.4 V, the area enclosed within the CV curves shrunk significantly indicating

decreasing capacitance. Therefore, although simulating the potential window beyond 0.4 V was possible, it would not meaningfully change the main observations of the study, but it would further increase the computational cost and time of the simulations.

3.5. Method of solution and data processing

The governing equations along with the initial and boundary conditions were solved using finite element methods in the COMSOL Multiphysics solver. The time-dependent solver proceeded at adaptive time steps controlled by an absolute tolerance of 0.01 for SPECS simulations and 0.001 for CV simulations.

The total current density $j_{T,n}(\mathbf{r}_{E/E}, t)$ at the electrode/electrolyte interface located at $\mathbf{r}_{E/E}$ was expressed as the sum of the EDL current density $j_{EDL,n}(\mathbf{r}_{E/E}, t)$ and the Faradaic current density $j_{F,n}(\mathbf{r}_{E/E}, t)$ so that $j_{T,n}(\mathbf{r}_{E/E}, t) = j_{EDL,n}(\mathbf{r}_{E/E}, t) + j_{F,n}(\mathbf{r}_{E/E}, t)$. The EDL current density $j_{EDL,n}(\mathbf{r}_{E/E}, t)$ was defined as [54],

$$j_{EDL,n}(\mathbf{r}_{E/E}, t) = -\epsilon_0 \epsilon_r \frac{\partial^2 \psi}{\partial n \partial t}(\mathbf{r}_{E/E}, t) \quad (17)$$

where $\epsilon_0 = 8.854 \times 10^{-12}$ F m⁻¹ is the vacuum permittivity. On the other hand, the Faradaic current density $j_{F,n}(\mathbf{r}_{E/E}, t)$ was computed from the generalized Frumkin–Butler–Volmer model evaluated at the electrode/electrolyte interface according to [7],

$$j_{F,n}(\mathbf{r}_{E/E}, t) = j_{F,0}(\mathbf{r}_{E/E}, t) \left\{ \exp \left[\frac{(1-\alpha)zF\eta(\mathbf{r}_{E/E}, t)}{R_u T} \right] - \exp \left[\frac{-\alpha zF\eta(\mathbf{r}_{E/E}, t)}{R_u T} \right] \right\} \quad (18)$$

where $j_{F,0}(\mathbf{r}_{E/E}, t)$ is the local exchange current density expressed as [49,50],

$$j_{F,0}(\mathbf{r}_{E/E}, t) = zFk_0 [c_1(\mathbf{r}_{E/E}, t)]^{1-\alpha} [c_{1,P,max} - c_{1,P}(\mathbf{r}_{E/E}, t)]^\alpha [c_{1,P}(\mathbf{r}_{E/E}, t)]^\alpha. \quad (19)$$

In addition, the surface overpotential $\eta(\mathbf{r}_{E/E}, t)$ necessary to drive the redox reactions at the electrode/electrolyte interface [Eq. (18)] was expressed as [7],

$$\eta(\mathbf{r}_{E/E}, t) = \Delta\psi_H(\mathbf{r}_{E/E}, t) - \Delta\psi_{eq}(t) \quad (20)$$

where $\Delta\psi_H(\mathbf{r}_{E/E}, t)$ is the local potential drop across the Stern layer at the electrode/electrolyte interface and $\Delta\psi_{eq}(t)$ is the equilibrium potential difference.

Finally, the current density $j(t)$ (in A/m²) averaged over the footprint surface area A_{fp} of the current collector was defined as [55],

$$j(t) = \frac{\iint_{A_{BET}} j_n(\mathbf{r}_{E/E}, t) dA_{BET}}{A_{fp}} \quad (21)$$

From the numerically simulated cyclic voltammograms, the differential capacitances associated with EDL formation at the geometric surface $C_{diff,1}(\psi_s)$ and at the porous surface $C_{diff,2}(\psi_s)$, defined per unit surface area A_{fp} of the current collector, were determined as [42],

$$C_{diff,i}(\psi_s) = \left| \frac{\iint_{A_{BET,i}} j_{EDL,n}(\mathbf{r}_{E/E}, \psi_s) dA_{BET,i}}{A_{fp}v} \right| \quad \text{with } i = 1 \text{ or } 2. \quad (22)$$

Moreover, the differential total EDL footprint capacitance $C_{diff,EDL}(\psi_s)$ was simply the sum of $C_{diff,1}(\psi_s)$ and $C_{diff,2}(\psi_s)$, i.e.,

$$C_{diff,EDL}(\psi_s) = C_{diff,1}(\psi_s) + C_{diff,2}(\psi_s). \quad (23)$$

3.6. SPECS fitting model

In the absence of residual current density (i.e., $j_r^S(t) = 0$) and combining Eqs. (2) and (10), the original fitting function of the SPECS method for the total footprint current density response to an imposed potential step $\Delta\psi_s$ in a porous pseudocapacitive electrode is such that [8–10],

$$j_T^S(t) = \frac{\Delta\psi_s}{R_1} \exp\left(-\frac{t}{R_1 C_1}\right) + \frac{\Delta\psi_s}{R_2} \exp\left(-\frac{t}{R_2 C_2}\right) + P_1 \exp(-P_2 t). \quad (24)$$

Here, superscript “S” refers to fitting functions of the different current densities in the original SPECS method in order to distinguish them from the numerical evaluations of $j_{EDL}(t)$, $j_F(t)$ and $j_T(t)$ obtained from simulations [Eqs. (17), (18), and (21)]. The fitting parameters $R_1(\psi_s)$, $R_2(\psi_s)$, $C_1(\psi_s)$, $C_2(\psi_s)$, $P_1(\psi_s)$, and $P_2(\psi_s)$ were determined by nonlinear least squares fitting of the footprint current densities at each potential step by minimizing the objective function δ defined as [56],

$$\delta = \sum_{i=1}^{N_s} \left\{ \left[j_T(t_i) - j_T^S(t_i) \right] \frac{\Delta t_i}{t_e} \right\}^2 \quad (25)$$

where $\Delta t_i = t_i - t_{i-1}$ is the adaptive time step. This definition of δ ensured that the results were unaffected by the exact size of the adaptive time steps taken by the time-dependent solver.

A genetic algorithm solver was used for this optimization problem [57]. For each fitting trial, the algorithm randomly generated an initial population of 200 fitting parameter values. During each generation, a portion of the existing population was selected, based on the objective function δ , to generate a new population of 200 fitting parameter values. Convergence was reached if (i) the average relative change in the best objective function δ over 200 generations was less than 10^{-5} , or (ii) 10^5 generations had been produced [57].

4. Results and discussion

4.1. SPECS simulation and original SPECS fitting model

Fig. 2(a) plots the temporal evolution of the imposed potential $\psi_s(0, y, z, t)$ given by Eq. (14) during a charging/discharging cycle for numerical simulations of the SPECS method. It involved a series of small potential steps of $\Delta\psi_s = 0.04$ V with equilibration time $t_e = 0.4$ s. To avoid discontinuity in the potential $\psi(\mathbf{r}, t)$ and the associated numerical instabilities at the transition from one step to another, the potential step was smoothed using a polynomial function with a continuous second order derivative during a transition time $t_t = 0.5$ ms, as developed previously [14].

Fig. 2(b) plots the numerically simulated total footprint current density $j_T(t)$ resulting from the imposed potential $\psi_s(0, y, z, t)$. Fig. 2 also plots the simulated footprint current densities due to (c) EDL formation $j_{EDL}(t)$ [Eqs. (17) and (21)] and (d) Faradaic reactions $j_F(t)$

[Eqs. (18) and (21)] such that $j_T(t) = j_{EDL}(t) + j_F(t)$. Here, the current densities were recorded at intervals based on adaptive time steps, giving 129 data points per potential step for the fitting analysis of the SPECS method.

Fig. 3 compares the numerically simulated Faradaic footprint current density $j_F(t)$ [Eqs. (18) and (21)] with the fitted current density $j_F^S(t)$ using the original SPECS fitting function [Eq. (10)] (a) at $\psi_s = 0.4$ V during charging and (b) at $\psi_s = 0$ V during discharging, with potential steps $\Delta\psi_s = 0.04$ V. Here, the simulated current density $j_F(t)$ showed significant discrepancies with the fitted current density $j_F^S(t)$ at both potentials. At $\psi_s = 0$ V in particular, the fitted Faradaic current density $j_F^S(t)$ failed to capture the spike and the rapid decay of the simulated current density $j_F(t)$ within 0.02 s after the imposed potential step. Fig. 3 then plots $\log|j_F(t)|$ as a function of time t (c) at $\psi_s = 0.4$ V during charging and (d) at $\psi_s = 0$ V during discharging. In both cases, $\log|j_F(t)|$ featured a clear change in slope during the potential step, and it approached separate asymptotes (dashed lines) on either side of this inflection point. This suggests that the Faradaic footprint current density $j_F(t)$ in a porous pseudocapacitive electrode featured two distinct relaxation time constants. Thus, the expression of Eq. (10), validated for planar electrodes, should be modified.

4.2. Modified SPECS fitting model

In light of the previous observations, the original SPECS fitting function given by Eq. (10) for the Faradaic footprint current density was revised to include two exponential decays, i.e.,

$$j_F^M(t) = j_{F1}^M(t) + j_{F2}^M(t) = P_1 \exp(-P_2 t) + P_3 \exp(-P_4 t) \quad (26)$$

where superscript “M” refers to the modified SPECS fitting model. Here, $j_{F1}^M(t)$ represents the surface-controlled Faradaic footprint current density due to reversible redox reactions occurring at or near the electrode/electrolyte interface and limited by interfacial charge transfer kinetics [5,58]. Similarly, $j_{F2}^M(t)$ represents the diffusion-controlled Faradaic footprint current density due to ion intercalation/deintercalation in/out of the electrode spherical particles and limited by solid state ion diffusion [5,58]. Thus, the fitting function of the SPECS method for the total footprint current density response to an imposed potential step $\Delta\psi_s$ in a porous pseudocapacitive electrode is now written as,

$$j_T^M(t) = \frac{\Delta\psi_s}{R_1} \exp\left(-\frac{t}{R_1 C_1}\right) + \frac{\Delta\psi_s}{R_2} \exp\left(-\frac{t}{R_2 C_2}\right) + P_1 \exp(-P_2 t) + P_3 \exp(-P_4 t). \quad (27)$$

The rest of the fitting procedure was the same as that previously described. Here, Eq. (27) included four time constants namely (i) the EDL time constant $\tau_{EDL1}(\psi_s) = R_1(\psi_s)C_1(\psi_s)$ associated with fast EDL formation at the so-called geometric surface, (ii) the EDL time constant $\tau_{EDL2}(\psi_s) = R_2(\psi_s)C_2(\psi_s)$ associated with slower EDL formation at the electrode/electrolyte interface within the porous electrode, (iii) the Faradaic time constant $\tau_{F1}(\psi_s) = 1/P_2(\psi_s)$ depending on the rate of interfacial charge transfer kinetics in surface-controlled Faradaic reactions, and (iv) the Faradaic time constant $\tau_{F2}(\psi_s) = 1/P_4(\psi_s)$ representing the diffusion time constant τ_d associated with diffusion-controlled Faradaic reactions [14]. As such, $\tau_{EDL1}(\psi_s)$ and $\tau_{F1}(\psi_s)$ were expected to be smaller than $\tau_{EDL2}(\psi_s)$ and $\tau_{F2}(\psi_s)$, respectively. The fitting parameters $R_1(\psi_s)$, $R_2(\psi_s)$, $C_1(\psi_s)$, $C_2(\psi_s)$, $P_2(\psi_s)$, and $P_4(\psi_s)$ were positive real numbers, while $P_1(\psi_s)$ and $P_3(\psi_s)$ were positive during charging and negative during discharging.

Fig. 4 compares the numerically simulated (a, b) total $j_T(t)$, (c, d) EDL $j_{EDL}(t)$, and (e, f) Faradaic $j_F(t)$ footprint current densities (same as in Fig. 2) with their respective fit (a, b) $j_T^M(t)$, (c, d) $j_{EDL}^M(t)$, and (e, f) $j_F^M(t)$ using the modified SPECS fitting function [Eq. (27)] at $\psi_s = 0.4$ V during charging and $\psi_s = 0$ V during discharging, with potential steps $\Delta\psi_s = 0.04$ V. Here, the numerically simulated current densities $j_T(t)$, $j_{EDL}(t)$, and $j_F(t)$ were closely matched by the fitted

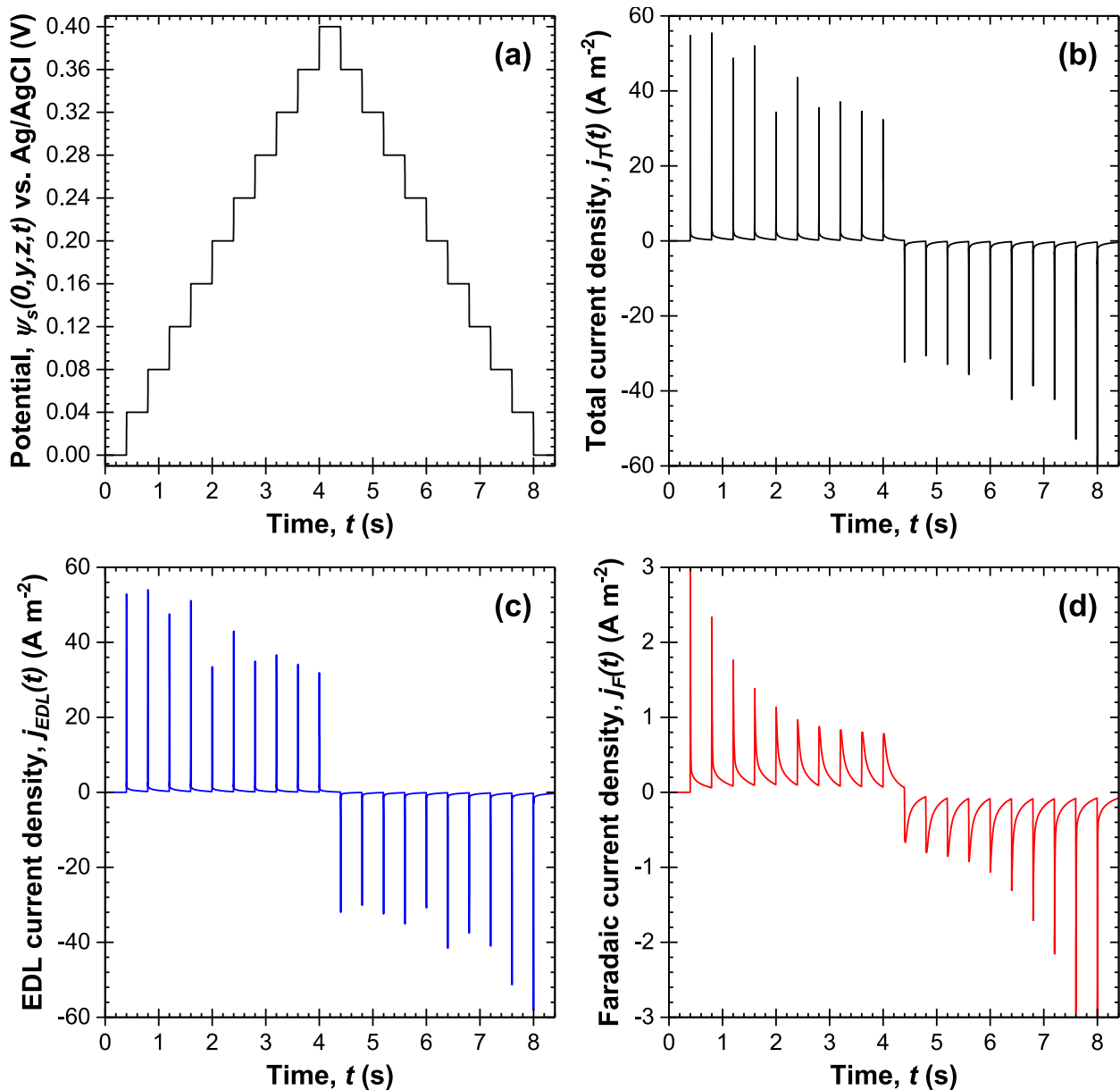


Fig. 2. Temporal evolution of (a) the imposed potential $\psi_s(0,y,z,t)$ [Eq. (14)] with step size $\Delta\psi_s = 0.04$ V and equilibration time $t_e = 0.4$ s and resulting (b) total $j_T(t)$, (c) EDL $j_{EDL}(t)$, and (d) Faradaic $j_F(t)$ footprint current densities [Eqs. (17), (18), and (21)] obtained with the SPECS method.

current densities $j_T^M(t)$, $j_{EDL}^M(t)$, and $j_F^M(t)$ retrieved from the modified SPECS fitting function at both potentials within the entire time range, unlike from the original SPECS fitting function (Fig. 3).

Fig. 5 plots the EDL footprint current densities at the geometric surface $j_{EDL1}^M(t)$ and at the porous surface $j_{EDL2}^M(t)$ as well as the surface-controlled $j_{F1}^M(t)$ and diffusion-controlled $j_{F2}^M(t)$ Faradaic footprint current densities [Eq. (27)] predicted by the modified SPECS fitting function at $\psi_s = 0.4$ V during charging and $\psi_s = 0$ V during discharging, with potential steps $\Delta\psi_s = 0.04$ V. Note that the fitted EDL $j_{EDL}^M(t)$ and Faradaic $j_F^M(t)$ footprint current densities are such that $j_{EDL}^M(t) = j_{EDL1}^M(t) + j_{EDL2}^M(t)$ and $j_F^M(t) = j_{F1}^M(t) + j_{F2}^M(t)$. Immediately after imposing a potential step, the footprint current densities featured a spike due to EDL formation, redox reactions, and ion intercalation/deintercalation in/out of the electrode spherical particles [14]. This spike was not captured by the fitting function due to the truncation performed to obtain Eq. (10) from Eq. (7). Afterwards, $j_{EDL1}(t)$ decayed

faster than $j_{EDL2}(t)$ with respect to time t as EDL was forming or dissolving faster at the geometric surface than at surfaces within the porous electrode. Therefore, as expected, the time constants were such that $\tau_{EDL1}(\psi_s) < \tau_{EDL2}(\psi_s)$ [8–10]. In addition, $j_{F1}(t)$ decayed rapidly at low potentials due to fast interfacial charge transfer kinetics in the Faradaic regime but slowly at high potentials due to slow kinetics in the capacitive regime [39]. By contrast, $j_{F2}(t)$ decayed slowly at all potentials due to consistently slow ion intercalation/deintercalation in/out of the electrode spherical particles and the relatively large time constant $\tau_{F2}(\psi_s)$.

4.3. SPECS fitting parameters interpretation

Fig. 6 plots the fitting parameters $R_1(\psi_s)$, $C_1(\psi_s)$, $R_2(\psi_s)$, and $C_2(\psi_s)$ associated with EDL formation while Fig. 7 plots $|P_1(\psi_s)|$, $P_2(\psi_s)$, $|P_3(\psi_s)|$, and $P_4(\psi_s)$ associated with Faradaic reactions of the modified

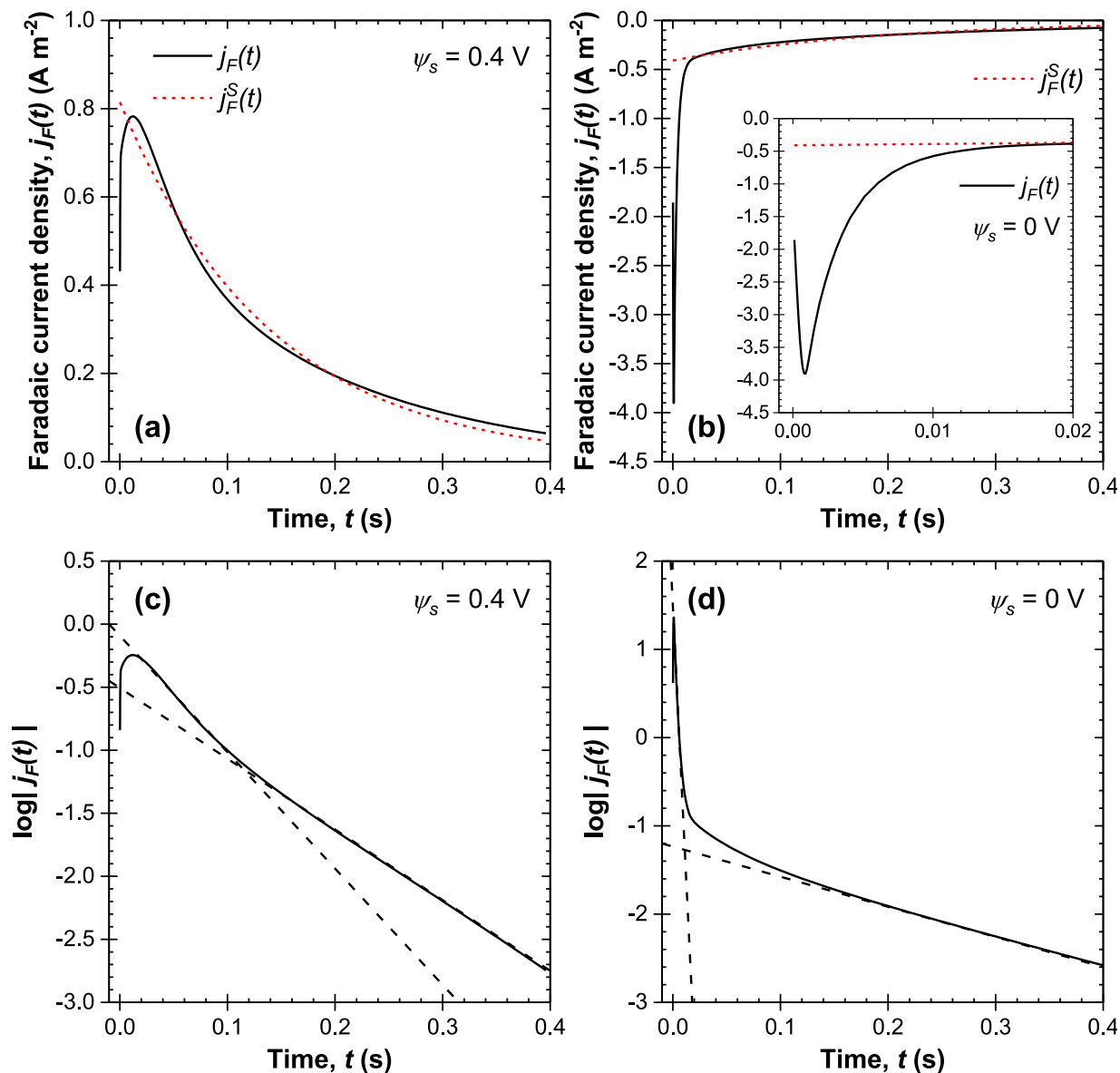


Fig. 3. Numerically simulated Faradaic footprint current density $j_F(t)$ [Eqs. (18) and (21)] and fitted current density $j_F^S(t)$ using the original SPECS fitting function [Eq. (24)] (a) at $\psi_s = 0.4$ V during charging and (b) at $\psi_s = 0$ V during discharging, with potential steps $\Delta\psi_s = 0.04$ V. (c, d) Data of (a, b) plotted as $\log|j_F(t)|$ vs. time t .

SPECS model as functions of potential ψ_s during a charging/discharging cycle between $\psi_{s,min} = 0$ V and $\psi_{s,max} = 0.4$ V with potential steps $\Delta\psi_s = 0.04$ V. First, all eight fitting parameters retrieved independently at each step formed continuous functions of ψ_s and their values obtained for the charging phase were similar to those of the discharging phase across the potential window. They were also approximately continuous functions of ψ_s , consistent with the results reported in our previous study [14].

Fig. 6(a) and (c) indicate that the footprint resistance $R_2(\psi_s)$ associated with the porous surface EDL was two orders of magnitude larger than $R_1(\psi_s)$ associated with the geometric surface EDL. Indeed, ions from the bulk electrolyte had to transport along tortuous paths through the porous electrode structure before reaching the surface of the particles, while they could reach the geometric surface from the bulk electrolyte without much resistance [8–10]. Similarly, Fig. 6(b) and (d) indicate that the porous surface EDL footprint capacitance $C_2(\psi_s)$ was one order of magnitude larger than the geometric surface EDL footprint capacitance $C_1(\psi_s)$. In fact, compared to the geometric surface, the porous surface accounted for the vast majority of the total

electrode/electrolyte interfacial area [8–10]. These results were consistent with the observations by Dupont and Donne [8–10]. Finally, Fig. 6(e) and (f) plot the geometric EDL time constant $\tau_{EDL1}(\psi_s) = R_1(\psi_s)C_1(\psi_s)$ and the porous EDL time constant $\tau_{EDL2}(\psi_s) = R_2(\psi_s)C_2(\psi_s)$. Here also, the values of each time constant were not only similar between charging and discharging but also relatively consistent across the entire potential window. This suggests that the kinetics of EDL formation, either at the interface of the electrode with the bulk electrolyte (geometric surface) or at the interfacial surface of micropores and mesopores within the porous electrode (porous surface), did not vary significantly with changing potential. Moreover, as expected, the geometric surface was more accessible than the porous surface such that at any potential $\tau_{EDL1}(\psi_s) < \tau_{EDL2}(\psi_s)$.

In order to investigate the influence of electrode particle layer number N on the fitting parameters, three cases were compared with $N = 2.5, 3.5,$ and 4.5 , respectively. Figure S5 in Supplementary Materials plots the four fitting parameters associated with EDL formation at the electrode/electrolyte interface: (a) $R_1(\psi_s)$, (b) $C_1(\psi_s)$, (c) $R_2(\psi_s)$,

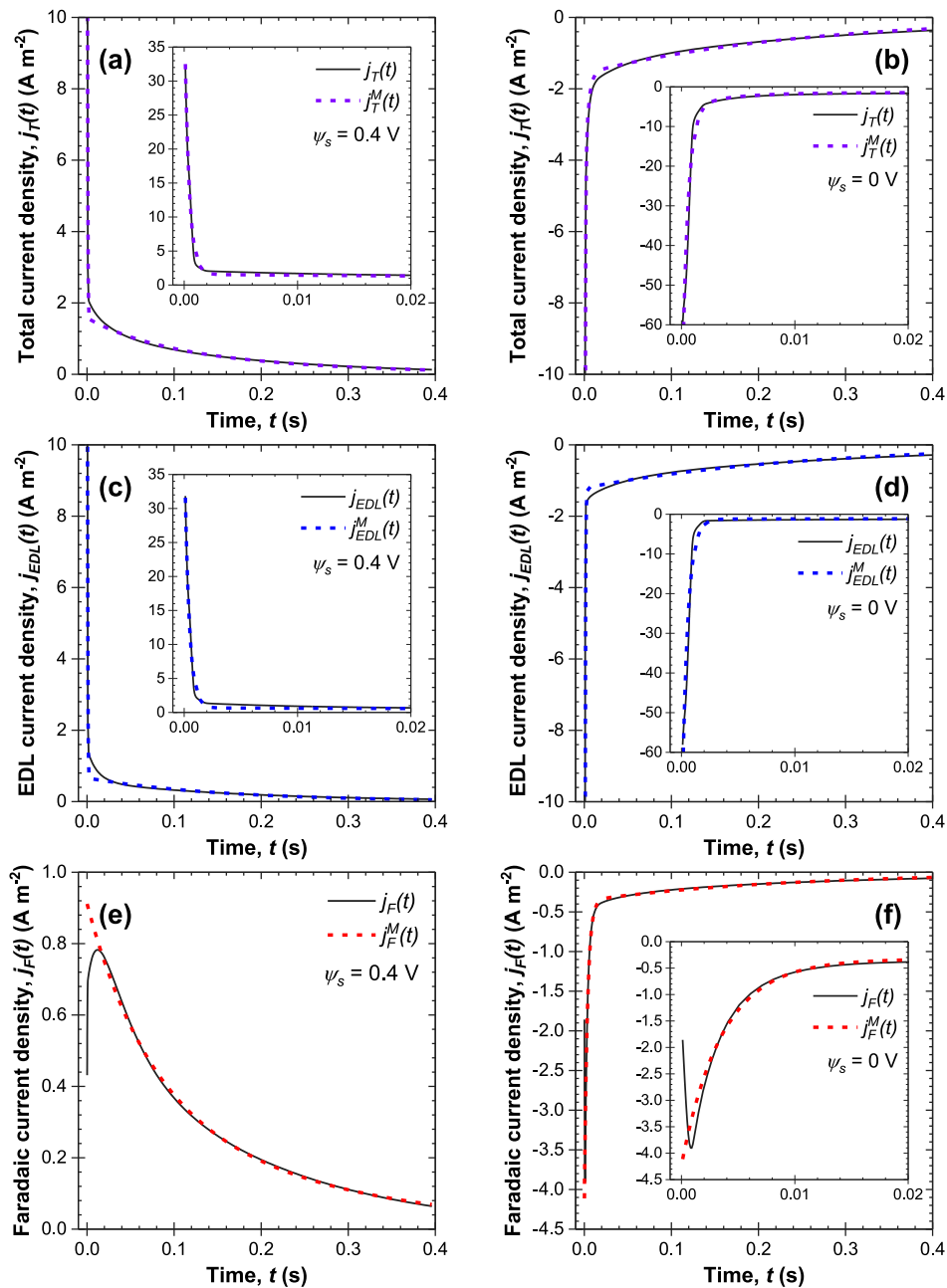


Fig. 4. Numerically simulated (a, b) total $j_T(t)$, (c, d) EDL $j_{EDL}(t)$, and (e, f) Faradaic $j_F(t)$ footprint current densities [Eqs. (17), (18), and (21)] along with their respective fit (a, b) $j_T^M(t)$, (c, d) $j_{EDL}^M(t)$, and (e, f) $j_F^M(t)$ using the modified SPECS fitting function [Eq. (27)] at $\psi_s = 0.4$ V during charging and at $\psi_s = 0$ V during discharging, with potential steps $\Delta\psi_s = 0.04$ V. Insets show the rapid changes between 0 and 0.02 s.

and (d) $C_2(\psi_s)$. Here, the porous surface area $A_{BET,2}$ increased with larger particle layer number [Fig. 1(c)]. For example, the three cases provided $A_{BET,2}$ of 176.7, 265.1, and 353.4 nm², respectively. As the porous surface area available for EDL formation increased, the porous surface EDL footprint capacitance $C_2(\psi_s)$ increased correspondingly [Figure S5(d)]. By contrast, the geometric surface area $A_{BET,1}$ remained the same at 44.2 nm² regardless of particle layer number [Fig. 1(b)]. Therefore, all three cases had similar geometric surface EDL footprint capacitances $C_1(\psi_s)$ [Figure S5(b)]. The same applied for the footprint resistances associated with the geometric surface $R_1(\psi_s)$ and the porous surface $R_2(\psi_s)$ EDL [Figures S5(a) and S5(c)], chiefly because the main factors contributing to the resistance of EDL formation, such as ion transport properties in the electrolyte, or the tortuosity of the porous

pseudocapacitive electrode, remained the same regardless of particle layer number.

Fig. 7(a) and (b) indicate that $|P_1(\psi_s)|$ and $P_2(\psi_s)$ were strongly dependent on the rate of interfacial charge transfer kinetics but were the same at any given potential ψ_s during charging and discharging. Indeed, the diminishing kinetics rate with increasing potential and the transition from the Faradaic to the capacitive regime led to a sharp decrease in both $|P_1(\psi_s)|$ and $P_2(\psi_s)$. In fact, according to our previous study [14] validating the original SPECS fitting function [Eq. (24)] for 1D planar pseudocapacitive electrodes, $|P_1(\psi_s)|$ was a function of both Λ and b_1 , while $P_2(\psi_s)$ was a function of b_1 only. Specifically, with increasing potential, the interfacial charge transfer resistance R_{ct} increased but the diffusion resistance R_d was relatively constant, such

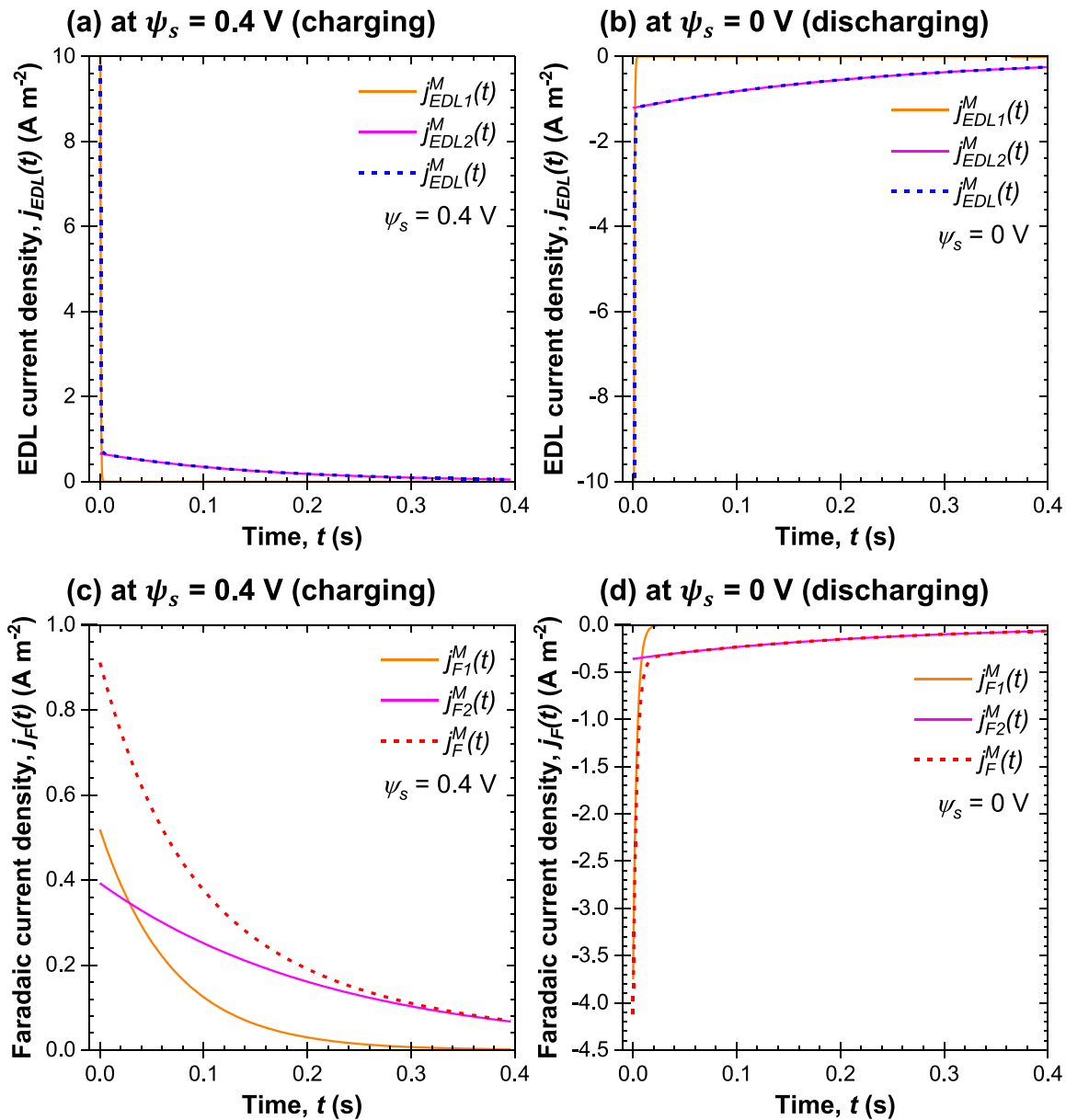


Fig. 5. EDL footprint current densities at the geometric surface $j_{EDL1}^M(t)$ and at the porous surface $j_{EDL2}^M(t)$ as well as surface-controlled $j_{F1}^M(t)$ and diffusion-controlled $j_{F2}^M(t)$ Faradaic footprint current densities [Eq. (27)] predicted by the modified SPECS fitting function (a, c) at $\psi_s = 0.4$ V during charging and (b, d) at $\psi_s = 0$ V during discharging, with potential steps $\Delta\psi_s = 0.04$ V. Note that the fitted EDL $j_{EDL}^M(t)$ and Faradaic $j_F^M(t)$ footprint current densities are such that $j_{EDL}^M(t) = j_{EDL1}^M(t) + j_{EDL2}^M(t)$ and $j_F^M(t) = j_{F1}^M(t) + j_{F2}^M(t)$.

that Λ decreased according to Eq. (9). This meant that b_1 , as the first root of Eq. (8), decreased as well. As a result, both $|P_1(\psi_s)|$ and $P_2(\psi_s)$ decreased sharply with increasing potential, according to Eq. (11). Finally, a parametric study was performed where the reaction rate constant k_0 varied between 10^{-10} and $10^{-8} m^{2.5} mol^{-0.5} s^{-1}$ for different cases. Here, increasing k_0 increased the rate of interfacial charge transfer kinetics and resulted in faster surface redox reactions. Consequently, both $|P_1(\psi_s)|$ and $P_2(\psi_s)$ increased. These results are described in detail in Supplementary Materials (see Section S.3.1).

Fig. 7(c) and (d) indicate that $|P_3(\psi_s)|$ and $P_4(\psi_s)$ did not vary significantly with changing potential. This suggests that the transport rate of ion intercalation/deintercalation in/out of the electrode spherical particles and the associated time constants were relatively constant across the entire potential window [39]. Indeed, the local concentration of Li^+ ions in the electrode $c_{1,p}(\mathbf{r}, t)$ was governed by the 3D transient mass diffusion equation (see Supplementary Materials) and the ion diffusion

coefficient was assumed to be constant with $D_{1,p} = 10^{-14} m^2 s^{-1}$ for the baseline case. Finally, a parametric study was performed where the ion diffusion coefficient $D_{1,p}$ varied between 10^{-14} and $10^{-12} m^2 s^{-1}$ for different cases. Here, increasing $D_{1,p}$ increased the rate of solid state ion diffusion. Consequently, both $|P_3(\psi_s)|$ and $P_4(\psi_s)$ increased. These results are described in detail in Supplementary Materials (see Section S.3.2).

Fig. 8(a) plots the numerically simulated cyclic voltammograms after imposing the potential $\psi_s(0, y, z, t)$ given by Eq. (15) in the same porous pseudocapacitive electrode as that simulated in Figs. 6 and 7. The potential window ranged from $\psi_{s,min} = 0$ V to $\psi_{s,max} = 0.4$ V, and the scan rate was chosen as $v = \Delta\psi_s/t_e = 0.1$ V s^{-1} , both consistent with the conditions in the SPECS simulations. The overall shapes of the simulated cyclic voltammograms were similar to those typically measured experimentally [59]. Fig. 8(b) and (c) compare the EDL footprint capacitances for the geometric surface

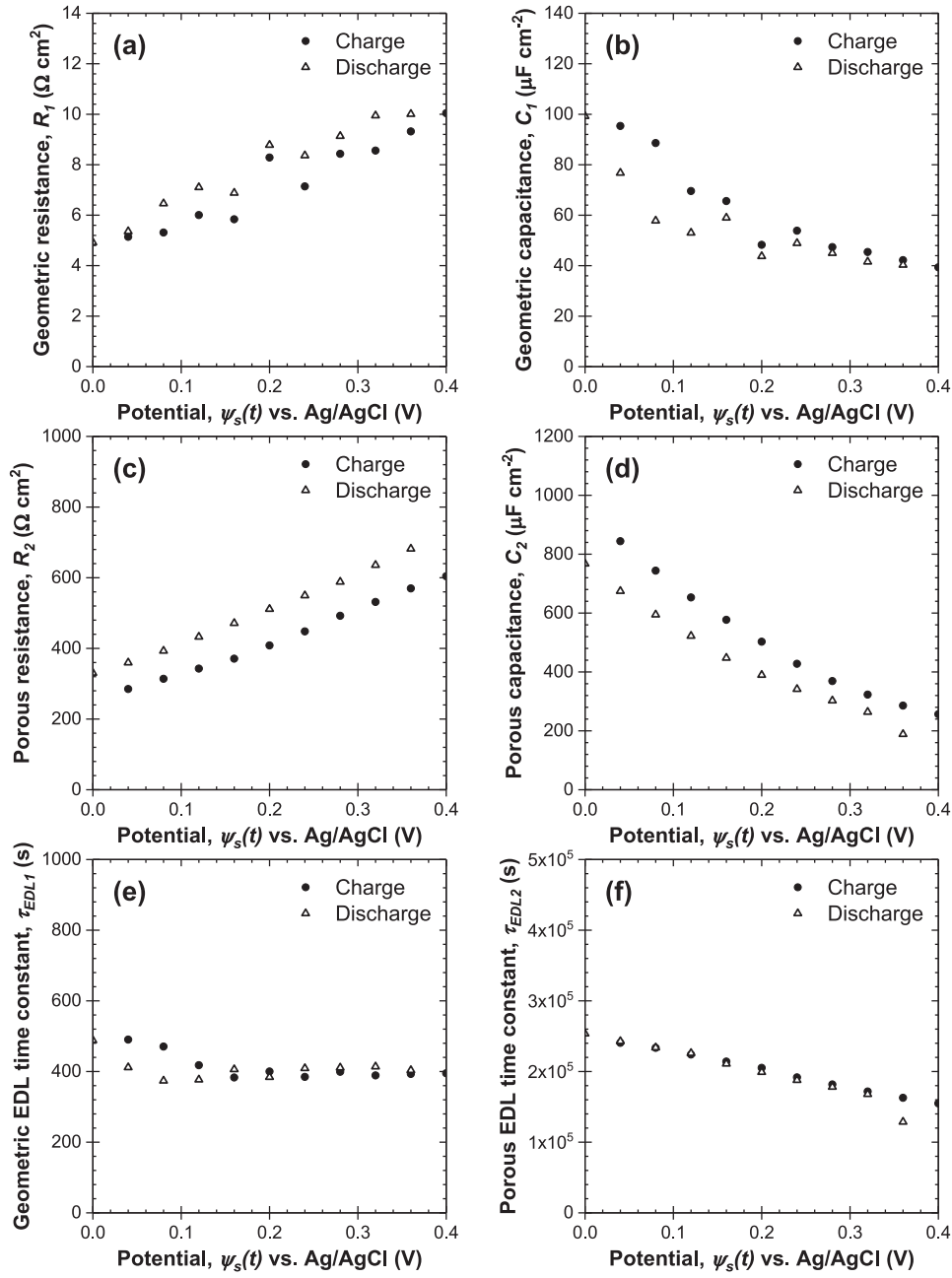


Fig. 6. Fitting parameters of the modified SPECS model associated with EDL formation (a) $R_1(\psi_s)$, (b) $C_1(\psi_s)$, (c) $R_2(\psi_s)$, and (d) $C_2(\psi_s)$ along with EDL time constants (e) $\tau_{EDL1}(\psi_s) = R_1(\psi_s)C_1(\psi_s)$ and (f) $\tau_{EDL2}(\psi_s) = R_2(\psi_s)C_2(\psi_s)$ as functions of potential ψ_s during a charging/discharging cycle between $\psi_{s,min} = 0$ V and $\psi_{s,max} = 0.4$ V with potential steps $\Delta\psi_s = 0.04$ V.

$C_1(\psi_s)$ and the porous surface $C_2(\psi_s)$ obtained from SPECS using the modified fitting function with the differential capacitances $C_{diff,1}(\psi_s)$ and $C_{diff,2}(\psi_s)$ calculated from cyclic voltammograms [Eq. (22)]. Good agreement was obtained between the two independent methods during both charging and discharging. Moreover, Fig. 8(d) compares the total EDL footprint capacitance $C_{EDL}(\psi_s)$ calculated as the sum of $C_1(\psi_s)$ and $C_2(\psi_s)$ [Eq. (3)] with the differential total EDL footprint capacitance $C_{diff,EDL}(\psi_s)$ calculated from cyclic voltammograms [Eq. (23)]. Here also, $C_{EDL}(\psi_s)$ was in good agreement with $C_{diff,EDL}(\psi_s)$ during both charging and discharging. These results demonstrate that the modified SPECS method [Eq. (27)] can accurately predict the contributions from EDL formation both at the geometric surface and at the porous surface to the differential EDL capacitance.

4.4. MUSCA method

The MUSCA method was applied to the various fitted footprint current densities $j_i^M(t)$ at a given scan rate ν to obtain the mean footprint current densities $j_i^A(\psi_s)$ at potential ψ_s expressed as,

$$j_i^A(\psi_s) = \frac{1}{t_\nu} \int_0^{t_\nu} j_i^M(t) dt \quad (28)$$

with subscript $i = T, EDL, EDL1, EDL2, F, F1, \text{ or } F2$. Then, cyclic voltammograms were reconstructed by plotting $j_i^A(\psi_s)$ vs. ψ_s . Finally, the integral footprint capacitance $C_{int,i}^A(\nu)$ associated with each charge storage mechanism at scan rate ν was determined as [42],

$$C_{int,i}^A(\nu) = \oint \frac{j_i^A(\psi_s)}{2\nu(\psi_{s,max} - \psi_{s,min})} d\psi_s. \quad (29)$$

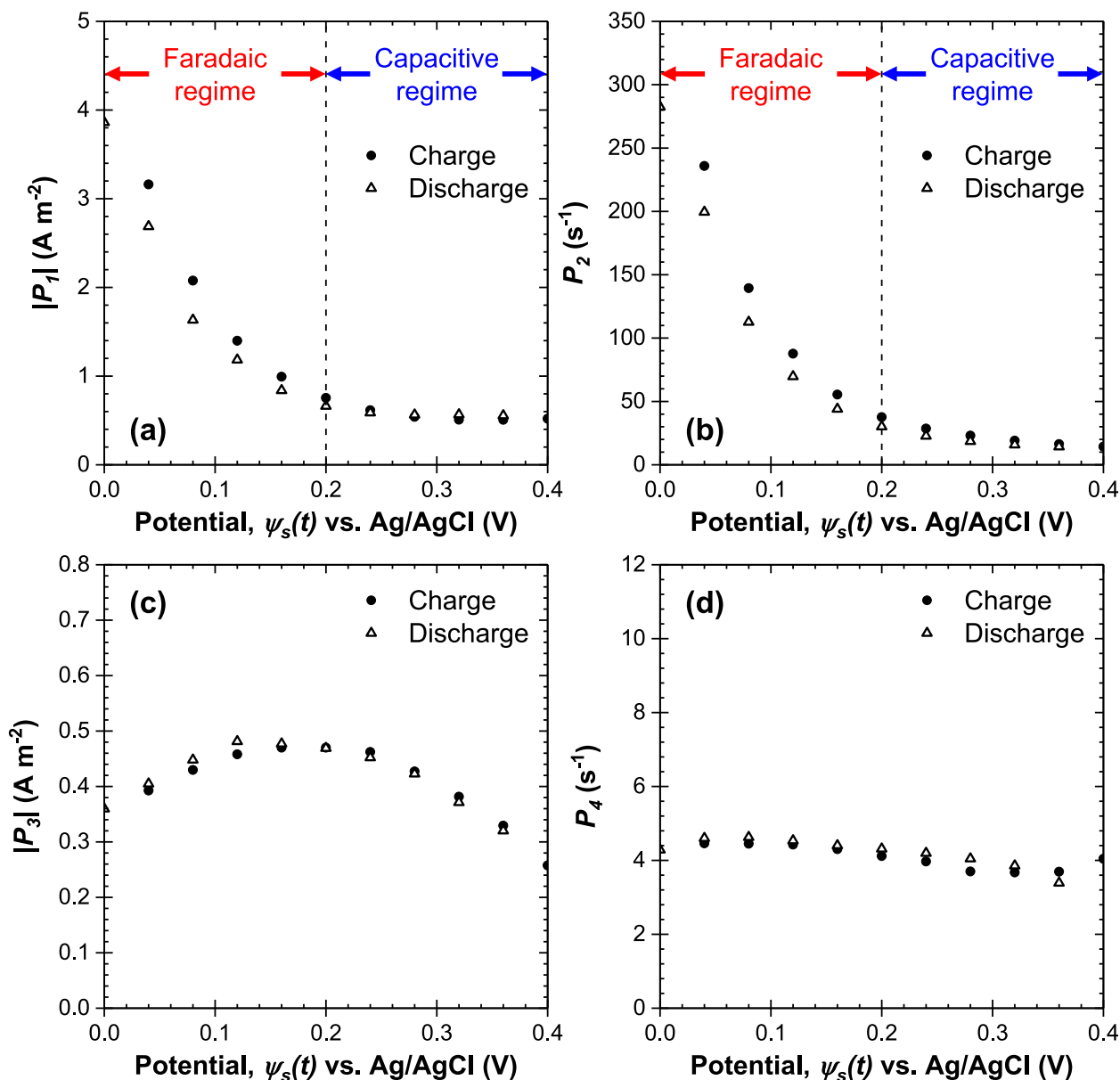


Fig. 7. Fitting parameters of the modified SPECS model associated with Faradaic reactions (a) $|P_1(\psi_s)|$, (b) $P_2(\psi_s)$, (c) $|P_3(\psi_s)|$, and (d) $P_4(\psi_s)$ as functions of potential ψ_s during a charging/discharging cycle between $\psi_{s,min} = 0$ V and $\psi_{s,max} = 0.4$ V with potential steps $\Delta\psi_s = 0.04$ V.

Fig. 9(a) indicates that the total $j_T^A(\psi_s)$, EDL $j_{EDL}^A(\psi_s)$, and Faradaic $j_F^A(\psi_s)$ mean footprint current densities obtained from the MUSCA method within the potential window from $\psi_{s,min} = 0$ V to $\psi_{s,max} = 0.4$ V at scan rate $\nu = 0.1$ V s⁻¹ were comparable with the numerically simulated cyclic voltammograms during both charging and discharging. Fig. 9(b) and (c) proceed to plot the reconstructed cyclic voltammograms associated with each charge storage mechanism at scan rates $\nu = 0.1$ V s⁻¹ and $\nu = 10$ V s⁻¹. Finally, Fig. 9(d) plots the corresponding integral footprint capacitance $C_{int,i}^A(\nu)$ for scan rates ν from 0.1 to 10 V s⁻¹ [Eq. (29)]. Note that the chosen scan rates were higher than those typically imposed in experimental measurements. This was attributed to the fact that the simulated electrode was thin and the influence of resistive losses and ion diffusion limitations only became apparent at such high scan rates. In fact, similar behavior was also observed in our previous studies simulating CV measurements in planar pseudocapacitive electrodes [37] and in

ordered carbon spheres EDLC electrodes [55]. Fig. 9(d) suggests that the integral total footprint capacitance $C_{int,T}^A(\nu)$ decreased with increasing scan rate. The integral geometric surface EDL footprint capacitance $C_{int,EDL1}^A(\nu)$ remained nearly constant across the range of scan rates considered. This was due to the fast transport and adsorption of ions at the geometric surface [60]. By contrast, the integral porous surface EDL footprint capacitance $C_{int,EDL2}^A(\nu)$ decreased monotonously with increasing scan rate due to slower ion transport through the tortuous porous electrode. On the other hand, the integral surface-controlled Faradaic footprint capacitance $C_{int,F1}^A(\nu)$ first remained constant, then decreased as the scan rate increased above 0.2 V s⁻¹ when the rate of interfacial charge transfer kinetics became limiting. Finally, the integral diffusion-controlled Faradaic footprint capacitance $C_{int,F2}^A(\nu)$ decreased monotonously with increasing scan rate due to rate-limited transport associated with solid state ion diffusion in the particle [60]. At low scan rates, EDL formation and diffusion-controlled Faradaic reactions

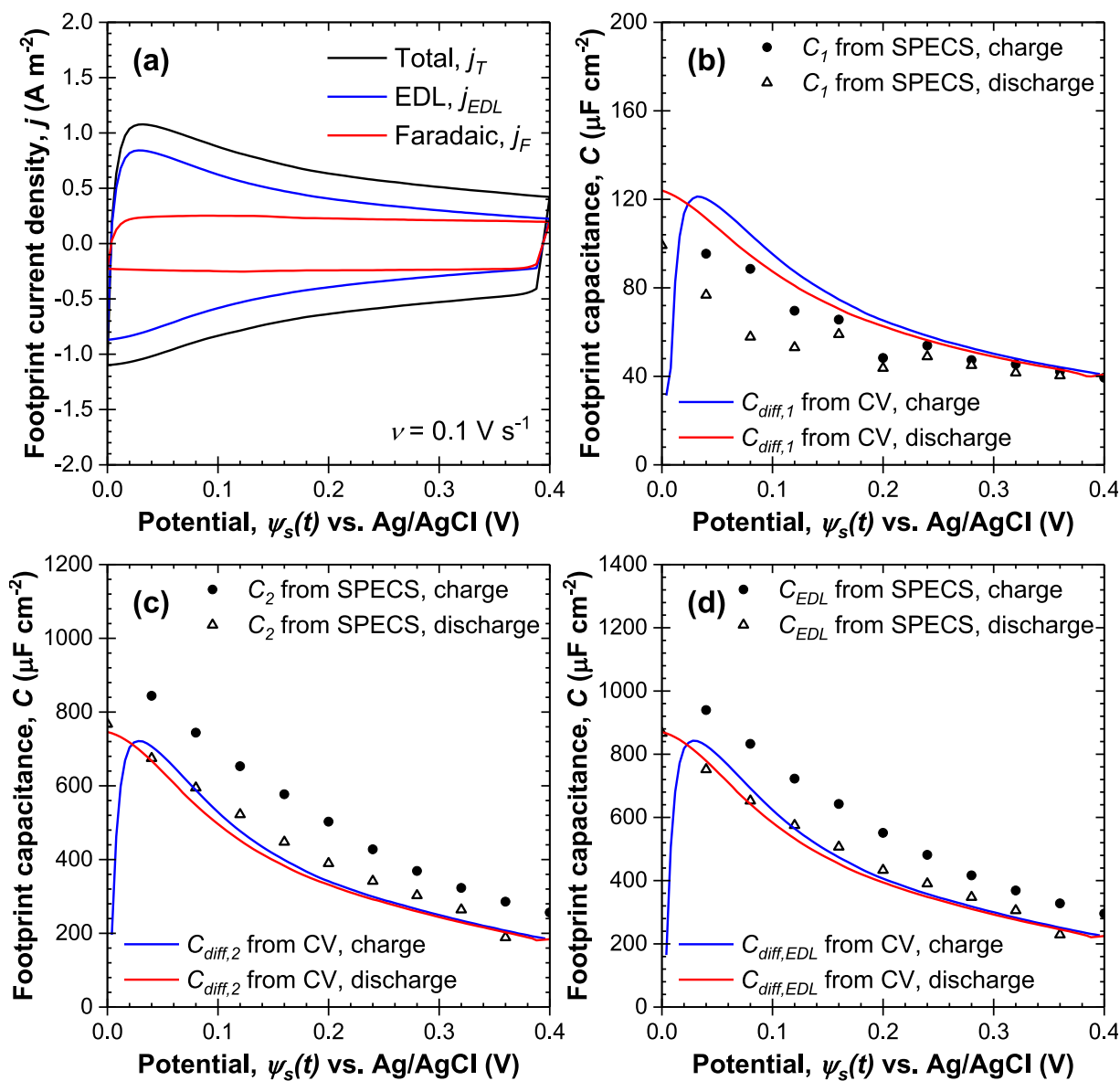


Fig. 8. (a) Numerically simulated cyclic voltammograms after imposing the potential $\psi_s(0, y, z, t)$ given by Eq. (15) in the porous pseudocapacitive electrode within a potential window from $\psi_{s,min} = 0$ V to $\psi_{s,max} = 0.4$ V at scan rate $\nu = 0.1$ V s⁻¹. Comparison of capacitances (b) $C_1(\psi_s)$, (c) $C_2(\psi_s)$, and (d) $C_{EDL}(\psi_s)$ obtained from SPECS using the modified fitting function with differential capacitances (b) $C_{diff,1}(\psi_s)$, (c) $C_{diff,2}(\psi_s)$, and (d) $C_{diff,EDL}(\psi_s)$ calculated from cyclic voltammograms [Eqs. (22) and (23)].

within the porous electrode contributed to the majority of the total charge storage. However, as the scan rate increased, EDL formation and Faradaic reactions at the geometric surface became the dominant charge storage mechanism.

5. Conclusion

In a previous study, we numerically validated the SPECS method proposed by Dupont and Donne [8–10] against numerical simulations for 1D planar pseudocapacitive electrodes. However, in this follow-up study, numerical simulations showed that the original SPECS fitting function could not adequately describe the current response in 3D porous pseudocapacitive electrodes. Therefore, the SPECS method was modified with a new fitting function to account for contributions from EDL formation at the electrode surface or at the electrode/electrolyte interface within the porous electrode, and from surface-controlled or diffusion-controlled Faradaic reactions. The modified SPECS method

was successfully validated against numerical simulations for 3D porous pseudocapacitive electrodes, based on the modified Poisson–Nernst–Planck (MPNP) model coupled with the Frumkin–Butler–Volmer theory to reproduce experimental data obtained from the SPECS method. Specifically, the numerically simulated total $j_T(t)$, EDL $j_{EDL}(t)$, and Faradaic $j_F(t)$ current densities were properly fitted by the current densities $j_T^M(t)$, $j_{EDL}^M(t)$, and $j_F^M(t)$ retrieved from the modified SPECS fitting function. Furthermore, the capacitances associated with EDL formation obtained from SPECS were in good agreement with those obtained from CV simulations. Finally, cyclic voltammograms were reconstructed from the MUSCA method. The integral capacitances associated with various charge storage mechanisms illustrated the faster kinetics of EDL formation at the geometric surface vs. at the porous surface, and the faster kinetics of surface-controlled vs. diffusion-controlled Faradaic reactions. Overall, this modified fitting function makes the SPECS method more accurate in distinguishing the different charge storage mechanisms in actual porous pseudocapacitive electrodes.

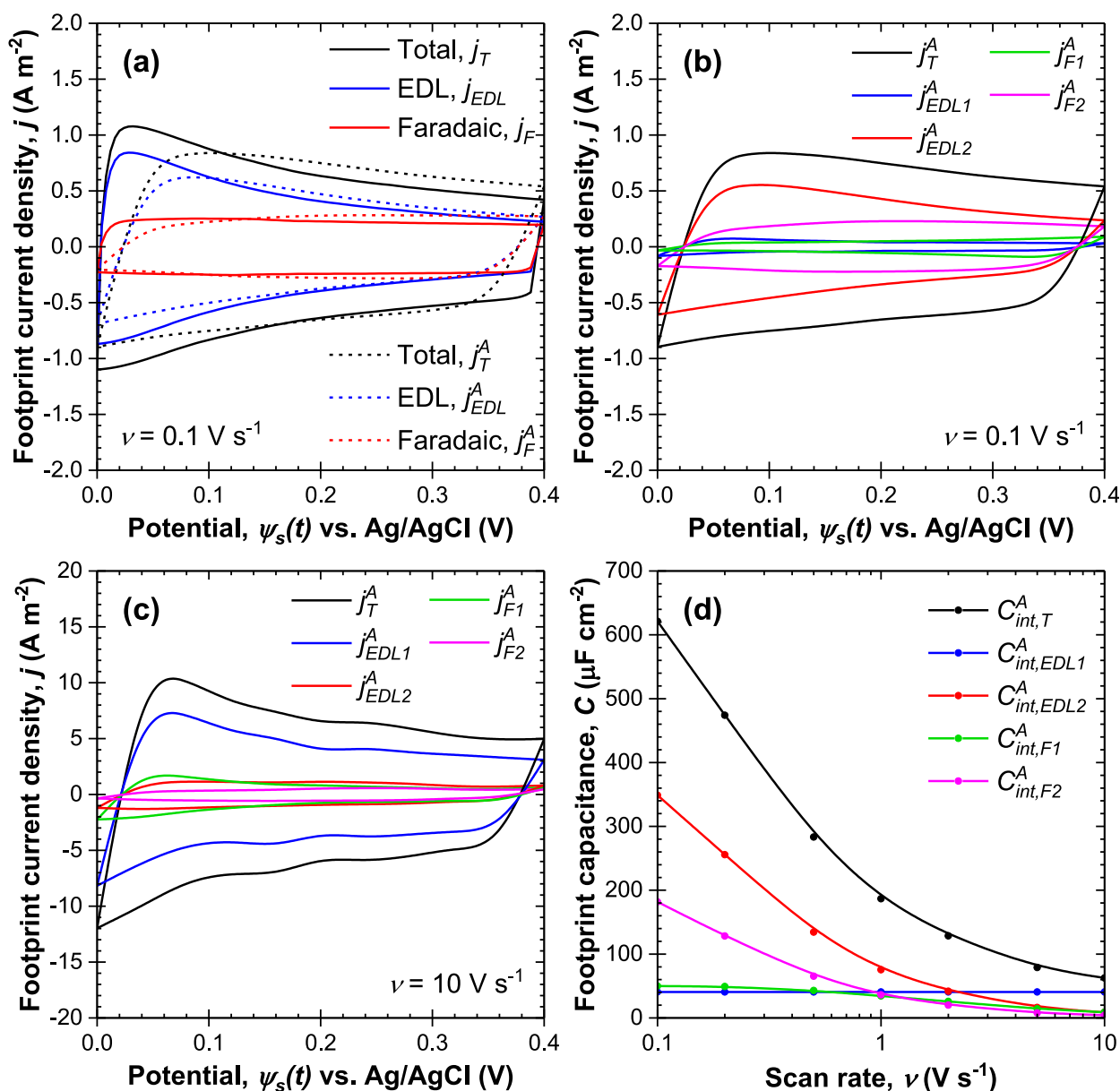


Fig. 9. (a) Comparison of total $j_T^A(\psi_s)$, EDL $j_{EDL}^A(\psi_s)$, and Faradaic $j_F^A(\psi_s)$ mean footprint current densities obtained from the MUSCA method [Eqs. (13) and (28)] with the numerically simulated cyclic voltammograms at scan rate $\nu = 0.1$ V s⁻¹. Reconstructed cyclic voltammograms associated with each charge storage mechanism at scan rates (b) $\nu = 0.1$ V s⁻¹ and (c) $\nu = 10$ V s⁻¹. (d) Corresponding integral footprint capacitance $C_{int,d}^A(\nu)$ for scan rates ν from 0.1 to 10 V s⁻¹ [Eq. (29)].

CRedit authorship contribution statement

Yucheng Zhou: Writing – review & editing, Writing – original draft, Visualization, Investigation, Formal analysis, Data curation, Conceptualization. **Matevž Frajnkovič:** Writing – review & editing, Investigation, Conceptualization. **Ampol Likitchawankun:** Writing – review & editing, Conceptualization. **Obaidallah Munteshari:** Conceptualization. **Bing-Ang Mei:** Conceptualization. **Laurent Pilon:** Writing – review & editing, Supervision, Project administration, Funding acquisition, Conceptualization.

Declaration of competing interest

The authors declare that they have no known competing financial interests or personal relationships that could have appeared to influence the work reported in this paper.

Data availability

Data will be made available on request.

Appendix A. Supplementary data

Supplementary material related to this article can be found online at <https://doi.org/10.1016/j.electacta.2024.144934>.

References

- [1] B.E. Conway, *Electrochemical Supercapacitors: Scientific Fundamentals and Technological Applications*, Springer, New York, NY, 1999.
- [2] B.E. Conway, V. Birss, J. Wojtowicz, The role and utilization of pseudocapacitance for energy storage by supercapacitors, *J. Power Sources* 66 (1–2) (1997) 1–14, [http://dx.doi.org/10.1016/S0378-7753\(96\)02474-3](http://dx.doi.org/10.1016/S0378-7753(96)02474-3).
- [3] M.R. Lukatskaya, B. Dunn, Y. Gogotsi, Multidimensional materials and device architectures for future hybrid energy storage, *Nature Commun.* 7 (1) (2016) 1–13, <http://dx.doi.org/10.1038/ncomms12647>.

- [4] M. Toupin, T. Brousse, D. Belanger, Charge storage mechanism of MnO₂ electrode used in aqueous electrochemical capacitor, *Chem. Mater.* 16 (16) (2004) 3184–3190, <http://dx.doi.org/10.1021/cm049649j>.
- [5] V. Augustyn, P. Simon, B. Dunn, Pseudocapacitive oxide materials for high-rate electrochemical energy storage, *Energy Environ. Sci.* 7 (5) (2014) 1597–1614, <http://dx.doi.org/10.1039/c3ee44164d>.
- [6] J.B. Cook, H.-S. Kim, T.C. Lin, C.-H. Lai, B. Dunn, S.H. Tolbert, Pseudocapacitive charge storage in thick composite MoS₂ nanocrystal-based electrodes, *Adv. Energy Mater.* 7 (2) (2017) 1601283, <http://dx.doi.org/10.1002/aenm.201601283>.
- [7] A.J. Bard, L.R. Faulkner, *Electrochemical Methods: Fundamentals and Applications*, John Wiley & Sons, New York, NY, 2000.
- [8] M.F. Dupont, S.W. Donne, Electrolytic manganese dioxide structural and morphological effects on capacitive performance, *Electrochim. Acta* 191 (2016) 479–490, <http://dx.doi.org/10.1016/j.electacta.2016.01.050>.
- [9] M.F. Dupont, S.W. Donne, Faradaic and non-faradaic contributions to the power and energy characteristics of electrolytic manganese dioxide for electrochemical capacitors, *J. Electrochem. Soc.* 163 (6) (2016) A888–A897, <http://dx.doi.org/10.1149/2.0401606jes>.
- [10] M.F. Dupont, S.W. Donne, Charge storage mechanisms in electrochemical capacitors: Effects of electrode properties on performance, *J. Power Sources* 326 (2016) 613–623, <http://dx.doi.org/10.1016/j.jpowsour.2016.03.073>.
- [11] H. Shao, Z. Lin, K. Xu, P.-L. Taberna, P. Simon, Electrochemical study of pseudocapacitive behavior of Ti₃C₂T_x MXene material in aqueous electrolytes, *Energy Storage Mater.* 18 (2019) 456–461, <http://dx.doi.org/10.1016/j.ensm.2018.12.017>.
- [12] M. Forghani, H. Mavroudis, J. McCarthy, S.W. Donne, Electroanalytical characterization of electrochemical capacitor systems using step potential electrochemical spectroscopy, *Electrochim. Acta* 332 (2020) 135508, <http://dx.doi.org/10.1016/j.electacta.2019.135508>.
- [13] M. Forghani, A.J. Roberts, Application of step potential electrochemical spectroscopy in pouch cell prototype capacitors, *Electrochim. Acta* 390 (2021) 138845, <http://dx.doi.org/10.1016/j.electacta.2021.138845>.
- [14] O. Munteshari, Y. Zhou, B.-A. Mei, L. Pilon, Theoretical validation of the step potential electrochemical spectroscopy (SPECS) and multiple potential step chronoamperometry (MUSCA) methods for pseudocapacitive electrodes, *Electrochim. Acta* 321 (2019) 134648, <http://dx.doi.org/10.1016/j.electacta.2019.134648>.
- [15] D. Belanger, T. Brousse, J.W. Long, Manganese oxides: Battery materials make the leap to electrochemical capacitors, *Electrochem. Soc. Interface* 17 (1) (2008) 49–52.
- [16] T. Brezesinski, J. Wang, S.H. Tolbert, B. Dunn, Ordered mesoporous α -MoO₃ with iso-oriented nanocrystalline walls for thin-film pseudocapacitors, *Nature Mater.* 9 (2) (2010) 146–151, <http://dx.doi.org/10.1038/nmat2612>.
- [17] J.B. Cook, H.-S. Kim, Y. Yan, J.S. Ko, S. Robbenolt, B. Dunn, S.H. Tolbert, Mesoporous MoS₂ as a transition metal dichalcogenide exhibiting pseudocapacitive Li and Na-ion charge storage, *Adv. Energy Mater.* 6 (9) (2016) 1501937, <http://dx.doi.org/10.1002/aenm.201501937>.
- [18] M.F. Dupont, S.W. Donne, Separating the faradaic and non-faradaic contributions to the total capacitance for different manganese dioxide phases, *J. Electrochem. Soc.* 162 (5) (2015) A5096–A5105, <http://dx.doi.org/10.1149/2.0161505jes>.
- [19] M.F. Dupont, S.W. Donne, Separating faradaic and non-faradaic charge storage contributions in activated carbon electrochemical capacitors using electrochemical methods: I. Step potential electrochemical spectroscopy, *J. Electrochem. Soc.* 162 (7) (2015) A1246–A1254, <http://dx.doi.org/10.1149/2.0611507jes>.
- [20] M.F. Dupont, S.W. Donne, A step potential electrochemical spectroscopy analysis of electrochemical capacitor electrode performance, *Electrochim. Acta* 167 (2015) 268–277, <http://dx.doi.org/10.1016/j.electacta.2015.03.137>.
- [21] E. Deiss, Spurious potential dependence of diffusion coefficients in Li⁺ insertion electrodes measured with PITT, *Electrochim. Acta* 47 (25) (2002) 4027–4034, [http://dx.doi.org/10.1016/S0013-4686\(02\)00363-8](http://dx.doi.org/10.1016/S0013-4686(02)00363-8).
- [22] C. Montella, Apparent diffusion coefficient of intercalated species measured with PITT: A simple formulation, *Electrochim. Acta* 51 (15) (2006) 3102–3111, <http://dx.doi.org/10.1016/j.electacta.2005.08.046>.
- [23] C. Montella, Discussion of the potential step method for the determination of the diffusion coefficients of guest species in host materials, *J. Electroanal. Chem.* 518 (2) (2002) 61–83, [http://dx.doi.org/10.1016/s0022-0728\(01\)00691-x](http://dx.doi.org/10.1016/s0022-0728(01)00691-x).
- [24] J. Li, F. Yang, X. Xiao, M.W. Verbrugge, Y.-T. Cheng, Potentiostatic intermittent titration technique (PITT) for spherical particles with finite interfacial kinetics, *Electrochim. Acta* 75 (2012) 56–61, <http://dx.doi.org/10.1016/j.electacta.2012.04.050>.
- [25] M.A. Hughes, J.A. Allen, S.W. Donne, Optimized electrolytic carbon and electrolyte systems for electrochemical capacitors, *ChemElectroChem* 7 (1) (2020) 266–282, <http://dx.doi.org/10.1002/celec.201901202>.
- [26] A.P. Cameron, S.B. Davey, K.G. Latham, S.W. Donne, Capacitive charge storage at the glassy carbon electrode: Comparison between aqueous and non-aqueous electrolytes, *J. Electrochem. Soc.* 168 (10) (2021) 100508, <http://dx.doi.org/10.1149/1945-7111/ac2a7d>.
- [27] M. Forghani, A.P. Cameron, S.W. Donne, Redox mechanism contributions to the behaviour of electrochemical capacitor materials, *J. Electrochem. Soc.* 168 (5) (2021) 050503, <http://dx.doi.org/10.1149/1945-7111/abf8d6>.
- [28] M. Forghani, J. McCarthy, A.P. Cameron, S.B. Davey, S.W. Donne, Semiconductor properties of electrodeposited manganese dioxide for electrochemical capacitors: Mott-Schottky analysis, *J. Electrochem. Soc.* 168 (2) (2021) 020508, <http://dx.doi.org/10.1149/1945-7111/abdde2>.
- [29] S.A. Abbas, M. Forghani, S. Anh, S.W. Donne, K.-D. Jung, Carbon hollow spheres as electrochemical capacitors: Mechanistic insights, *Energy Storage Mater.* 24 (2020) 550–556, <http://dx.doi.org/10.1016/j.ensm.2019.06.034>.
- [30] T. Wang, R.L. Sacci, J. Liang, C.-L. Do-Thanh, J. Fan, H. Chen, Y. Sun, B.P. Thapaliya, S.M. Mahurin, M. Zhou, J. Wu, S.W. Donne, S. Dai, Mechanistic insights of pore contributions in carbon supercapacitors by modified step potential electrochemical spectroscopy, *J. Electrochem. Soc.* 168 (6) (2021) 060530, <http://dx.doi.org/10.1149/1945-7111/ac099a>.
- [31] R. Qiao, N.R. Aluru, Ion concentrations and velocity profiles in nanochannel electroosmotic flows, *J. Chem. Phys.* 118 (10) (2003) 4692–4701, <http://dx.doi.org/10.1063/1.1543140>.
- [32] M.Z. Bazant, M.S. Kilic, B.D. Storey, A. Ajdari, Towards an understanding of induced-charge electrokinetics at large applied voltages in concentrated solutions, *Adv. Colloid Interface Sci.* 152 (1–2) (2009) 48–88, <http://dx.doi.org/10.1016/j.cis.2009.10.001>.
- [33] J.H. Masliyah, S. Bhattacharjee, *Electrokinetic and Colloid Transport Phenomena*, John Wiley & Sons, New York, NY, 2006.
- [34] H. Wang, L. Pilon, Mesoscale modeling of electric double layer capacitors with three-dimensional ordered structures, *J. Power Sources* 221 (2013) 252–260, <http://dx.doi.org/10.1016/j.jpowsour.2012.08.002>.
- [35] M.Z. Bazant, K. Thornton, A. Ajdari, Diffuse-charge dynamics in electrochemical systems, *Phys. Rev. E* 70 (2) (2004) 021506, <http://dx.doi.org/10.1103/PhysRevE.70.021506>.
- [36] H. Wang, A. Thiele, L. Pilon, Simulations of cyclic voltammetry for electric double layers in asymmetric electrolytes: A generalized modified Poisson-Nernst-Planck model, *J. Phys. Chem. C* 117 (36) (2013) 18286–18297, <http://dx.doi.org/10.1021/jp402181e>.
- [37] H.-L. Girard, B. Dunn, L. Pilon, Simulations and interpretation of three-electrode cyclic voltammograms of pseudocapacitive electrodes, *Electrochim. Acta* 211 (2016) 420–429, <http://dx.doi.org/10.1016/j.electacta.2016.06.066>.
- [38] B.-A. Mei, J. Lau, T. Lin, S.H. Tolbert, B.S. Dunn, L. Pilon, Physical interpretations of electrochemical impedance spectroscopy of redox active electrodes for electrical energy storage, *J. Phys. Chem. C* 122 (43) (2018) 24499–24511, <http://dx.doi.org/10.1021/acs.jpcc.8b05241>.
- [39] H.-L. Girard, H. Wang, A. d'Entremont, L. Pilon, Physical interpretation of cyclic voltammetry for hybrid pseudocapacitors, *J. Phys. Chem. C* 119 (21) (2015) 11349–11361, <http://dx.doi.org/10.1021/acs.jpcc.5b00641>.
- [40] H.-L. Girard, H. Wang, A.L. d'Entremont, L. Pilon, Enhancing faradaic charge storage contribution in hybrid pseudocapacitors, *Electrochim. Acta* 182 (2015) 639–651, <http://dx.doi.org/10.1016/j.electacta.2015.09.070>.
- [41] B.-A. Mei, B. Li, J. Lin, L. Pilon, Multidimensional cyclic voltammetry simulations of pseudocapacitive electrodes with a conducting nanorod scaffold, *J. Electrochem. Soc.* 164 (13) (2017) A3237–A3252, <http://dx.doi.org/10.1149/2.1241713jes>.
- [42] H. Wang, L. Pilon, Physical interpretation of cyclic voltammetry for measuring electric double layer capacitances, *Electrochim. Acta* 64 (2012) 130–139, <http://dx.doi.org/10.1016/j.electacta.2011.12.118>.
- [43] A.M. Colclasure, R.J. Kee, Thermodynamically consistent modeling of elementary electrochemistry in lithium-ion batteries, *Electrochim. Acta* 55 (28) (2010) 8960–8973, <http://dx.doi.org/10.1016/j.electacta.2010.08.018>.
- [44] P. Guillemet, T. Brousse, O. Crosnier, Y. Dandeville, L. Athouel, Y. Scudeller, Modeling pseudocapacitance of manganese dioxide, *Electrochim. Acta* 67 (2012) 41–49, <http://dx.doi.org/10.1016/j.electacta.2012.01.110>.
- [45] Q. Zhong, B. Huang, J. Ma, H. Li, Experimental study on relationship between SOC and OCV of lithium-ion batteries, *Int. J. Smart Grid Clean Energy* 3 (2) (2014) 149–153, <http://dx.doi.org/10.12720/sgce.3.2.149-153>.
- [46] G.J. Janz, R.P.T. Tomkins, *Nonaqueous Electrolytes Handbook*, Academic Press, New York, NY, 1972.
- [47] K. Nishikawa, Y. Fukunaka, T. Sakka, Y.H. Ogata, J.R. Selman, Measurement of LiClO₄ diffusion coefficient in propylene carbonate by Moire pattern, *J. Electrochem. Soc.* 153 (5) (2006) A830–A834, <http://dx.doi.org/10.1149/1.2178648>.
- [48] L.L. Zhang, X.S. Zhao, Carbon-based materials as supercapacitor electrodes, *Chem. Soc. Rev.* 38 (9) (2009) 2520–2531, <http://dx.doi.org/10.1039/b813846j>.
- [49] V.R. Subramanian, V. Boovaragavan, V. Ramadesigan, M. Arabandi, Mathematical model reformulation for lithium-ion battery simulations: Galvanostatic boundary conditions, *J. Electrochem. Soc.* 156 (4) (2009) A260–A271, <http://dx.doi.org/10.1149/1.3065083>.
- [50] G.M. Goldin, A.M. Colclasure, A.H. Wiedemann, R.J. Kee, Three-dimensional particle-resolved models of Li-ion batteries to assist the evaluation of empirical parameters in one-dimensional models, *Electrochim. Acta* 64 (2012) 118–129, <http://dx.doi.org/10.1016/j.electacta.2011.12.119>.
- [51] T.R. Jow, J.P. Zheng, Electrochemical capacitors using hydrous ruthenium oxide and hydrogen inserted ruthenium oxide, *J. Electrochem. Soc.* 145 (1) (1998) 49–52, <http://dx.doi.org/10.1149/1.1838209>.

- [52] H. Kim, B.N. Popov, A mathematical model of oxide/carbon composite electrode for supercapacitors, *J. Electrochem. Soc.* 150 (9) (2003) 1153–1160, <http://dx.doi.org/10.1149/1.1593039>.
- [53] G. Sikha, R.E. White, B.N. Popov, A mathematical model for a lithium-ion battery/electrochemical capacitor hybrid system, *J. Electrochem. Soc.* 152 (8) (2005) 1682–1693, <http://dx.doi.org/10.1149/1.1940749>.
- [54] H. Cohen, J.W. Cooley, The numerical solution of the time-dependent Nernst-Planck equations, *Biophys. J.* 5 (2) (1965) 145–162, [http://dx.doi.org/10.1016/S0006-3495\(65\)86707-8](http://dx.doi.org/10.1016/S0006-3495(65)86707-8).
- [55] B.-A. Mei, L. Pilon, Three-dimensional cyclic voltammetry simulations of EDLC electrodes made of ordered carbon spheres, *Electrochim. Acta* 255 (2017) 168–178, <http://dx.doi.org/10.1016/j.electacta.2017.09.060>.
- [56] C.T. Kelley, *Iterative Methods for Optimization*, Society for Industrial and Applied Mathematics, Philadelphia, PA, 1999.
- [57] D.E. Goldberg, *Genetic Algorithms in Search, Optimization, and Machine Learning*, Addison-Wesley Publishing Company, Boston, MA, 1989.
- [58] V. Augustyn, J. Come, M.A. Lowe, J.W. Kim, P.-L. Taberna, S.H. Tolbert, H.D. Abruna, P. Simon, B. Dunn, High-rate electrochemical energy storage through Li⁺ intercalation pseudocapacitance, *Nature Mater.* 12 (6) (2013) 518–522, <http://dx.doi.org/10.1038/nmat3601>.
- [59] Y. Gogotsi, R.M. Penner, Energy storage in nanomaterials - capacitive, pseudo-capacitive, or battery-like? *ACS Nano* 12 (3) (2018) 2081–2083, <http://dx.doi.org/10.1021/acsnano.8b01914>.
- [60] M. Forghani, S.W. Donne, Method comparison for deconvoluting capacitive and pseudo-capacitive contributions to electrochemical capacitor electrode behavior, *J. Electrochem. Soc.* 165 (3) (2018) A664–A673, <http://dx.doi.org/10.1149/2.0931803jes>.